

RESEARCH

Open Access



Kaempferol enhances ER-mitochondria coupling and protects motor neurons from mitochondrial dysfunction and ER stress in *C9ORF72*-ALS

Federica Pilotto^{3,4}, Paulien Hermine Smeele^{1,2}, Olivier Scheidegger³, Rim Diab⁴, Martina Schobesberger⁴, Julieth Andrea Sierra-Delgado^{1,2} and Smita Saxena^{1,2,4*}

Abstract

Repeat expansions in the *C9ORF72* gene are a frequent cause of amyotrophic lateral sclerosis (ALS) and frontotemporal dementia. Considerable progress has been made in identifying *C9ORF72*-mediated disease and resolving its underlying etiopathogenesis. The contributions of intrinsic mitochondrial deficits as well as chronic endoplasmic reticulum stress to the development of the *C9ORF72*-linked pathology are well established. Nevertheless, to date, no cure or effective therapy is available, and thus attempts to find a potential drug target, have received increasing attention. Here, we investigated the mode of action and therapeutic effect of a naturally occurring dietary flavanol, kaempferol in preclinical rodent and human models of *C9ORF72*-ALS. Notably, kaempferol treatment of *C9ORF72*-ALS human patient-derived motor neurons/neurons, resolved mitochondrial deficits, promoted resiliency against severe ER stress, and conferred neuroprotection. Treatment of symptomatic *C9ORF72* mice with kaempferol, normalized mitochondrial calcium uptake, restored mitochondria function, and diminished ER stress. Importantly, in vivo, chronic kaempferol administration ameliorated pathological motor dysfunction and inhibited motor neuron degeneration, highlighting the translational potential of kaempferol. Lastly, in silico modelling identified a novel kaempferol target and mechanistically the neuroprotective mechanism of kaempferol is through the iP3R-VDAC1 pathway via the modulation of GRP75 expression. Thus, kaempferol holds great promise for treating neurodegenerative diseases where both mitochondrial and ER dysfunction are causally linked to the pathophysiology.

*Correspondence:

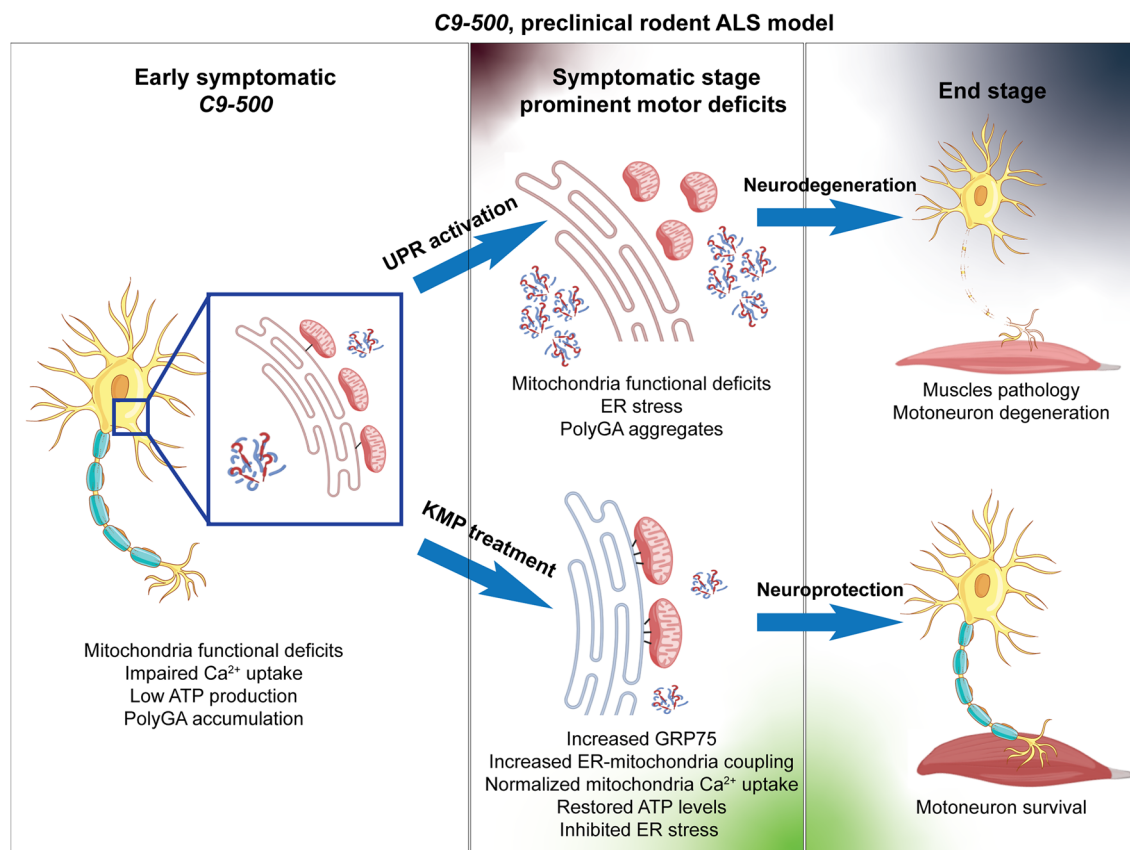
Smita Saxena
smitasaxena@missouri.edu

Full list of author information is available at the end of the article



© The Author(s) 2025. **Open Access** This article is licensed under a Creative Commons Attribution-NonCommercial-NoDerivatives 4.0 International License, which permits any non-commercial use, sharing, distribution and reproduction in any medium or format, as long as you give appropriate credit to the original author(s) and the source, provide a link to the Creative Commons licence, and indicate if you modified the licensed material. You do not have permission under this licence to share adapted material derived from this article or parts of it. The images or other third party material in this article are included in the article's Creative Commons licence, unless indicated otherwise in a credit line to the material. If material is not included in the article's Creative Commons licence and your intended use is not permitted by statutory regulation or exceeds the permitted use, you will need to obtain permission directly from the copyright holder. To view a copy of this licence, visit <http://creativecommons.org/licenses/by-nc-nd/4.0/>.

Graphical abstract



Introduction

Current research has highlighted that dysregulated ER stress and associated unfolded protein response (UPR) signaling are the leading cellular impairments contributing to the main pathogenic mechanism in neurodegeneration [1–4]. In the context of amyotrophic lateral sclerosis (ALS), motor neurons (MNs) are selectively prone to ER stress, influencing disease manifestation and kinetics [5–7]. Importantly, a hexanucleotide repeat expansion (HRE) in the first intronic region of the *C9ORF72* gene accounts for over 40% of all known familial and 10% of known sporadic forms of ALS. In healthy individuals, approximately 20–24 copies of the GGGGCC (G_4C_2) HRE are observed within the first intron of the *C9ORF72* gene. However, in disease, this G_4C_2 sequence is expanded and can range from hundreds to thousands of repeats. This specific intronic HRE leads to the development of three mutually non-exclusive pathological hallmarks, eventually resulting in the appearance of a spectrum disorder; *C9ORF72*-ALS/frontal temporal dementia (FTD). Firstly, the HRE has been shown to cause haploinsufficiency of the *C9ORF72* gene, leading to reduced *C9ORF72* RNA

and protein expression. Secondly, there is a gain of toxic function due to the bidirectional transcription of the G_4C_2 HRE, which produces toxic G_4C_2 and G_4C_2 repeat RNA species. Lastly, there is a gain of toxic function via the non-ATG mediated RAN translation of repeat RNAs to produce five different toxic dipeptide repeat proteins (Poly(GA), Poly(GR), Poly(GP), Poly(PR), and Poly(PA)), which act on and damage multiple cellular processes [8–10].

C9ORF72 induced pluripotent stem cells (iPSC)-derived motor neurons (iMNs), exhibit increased endoplasmic reticulum (ER) stress, together with reduced mitochondrial membrane potential, concomitant impairment in calcium (Ca^{2+}) homeostasis and reduced levels of the antiapoptotic protein Bcl-2 [6, 7, 11]. Additionally, *C9ORF72* is majorly a cytosolic protein, which has also been shown to localize to the mitochondrial inner membrane, where it has a function in controlling the process of oxidative phosphorylation, thus maintaining, and regulating cellular energy production and balance [12]. Thus, emerging evidence suggests that ER stress signaling, and mitochondrial

dysfunction are intricately associated with the pathophysiological manifestations linked to *C9ORF72*-ALS. One likely region of membrane contacts where the mitochondria are reversibly tethered to the ER are regions termed “Mitochondria-associated membranes (MAMs),” which play a crucial regulatory role in the supply of Ca^{2+} from the ER to mitochondria. These sites are critical for the rapid Ca^{2+} uptake by mitochondria through voltage-dependent anion channels (VDACs) located at the outer mitochondrial membrane (OMM) [13]. Moreover, MAMs have been implicated in the regulation of Ca^{2+} homeostasis, mitochondrial function, autophagy, apoptosis, and glucose homeostasis [14]. Within the context of ALS, mutations, MAM localized, and functioning proteins such as VAPB and Sig1R are known to cause familial ALS (fALS). The point mutation P56S in *VAPB*^{P56S} causes increased binding to the mitochondrial protein tyrosine phosphatase interacting protein 51 (PTPIP51), which causes reduced ER-mitochondria contacts, enhanced Ca^{2+} release from the ER and aberrant MAM morphology, and mitochondrial dysfunction [15].

A recent study from our group revealed the existence of an ER stress-mediated adaptive response in *C9ORF72* patient MNs, which was observed by the early yet transient increase in the expression of the MAM-localized chaperone GRP75. Transient GRP75 expression augmented ER-mitochondrial association, boosting mitochondrial function, and sustaining cellular bioenergetics during the initial stage of disease, thereby neutralizing early mitochondrial deficits. The gradual emergence of Poly(GA) aggregates led to the sequestration of GRP75, causing a subsequent loss of function at the MAM, resulting in mitochondrial Ca^{2+} uptake impairments and mitochondrial dysfunction in both human patient-derived and rodent MNs [7]. Similarly, another recent study showed that dysfunctional ER-mitochondria signaling and the disruption of VAPB-PTPIP51 tethers in *C9ORF72* patient-derived neurons and mutant *C9orf72* transgenic mice occurred presymptomatically and contributed to the pathogenic process. These impairments were linked to the expression of DPRs, which disrupted the VAPB-PTPIP51 interaction at the ER-mitochondria contacts and that may involve activation of glycogen synthase kinases-3 β , a known negative regulator of VAPB-PTPIP51 binding [16].

Therapeutic agents harboring the potential to simultaneously target both ER stress and mitochondrial function hold great promise as future therapeutic targets in neurodegenerative diseases and more so in ALS. Kaempferol (KMP) is a naturally occurring dietary flavanol, present in fruits and vegetables and has been shown to possess ER stress-inhibitory activity in cultured

mammalian cells [17, 18] and mice [19], anti-neuroinflammatory activity in rat models of ischemic stroke [20], mitochondrial Ca^{2+} uniporter channel activator [21] and ameliorated energy metabolism and symptomatic behavior in a rat model of traumatic brain injury [22]. While KMP has been predominantly studied as a potential tumor suppressor [19, 23–25], higher intake of KMP and other flavanols, was shown to be inversely correlated with the incidence of Alzheimer’s disease [26], emphasizing the neuroprotective potential of KMP in neurodegenerative diseases.

We here identify that KMP exerts a neuroprotective effect on *C9ORF72* ALS neurons by sustaining mitochondrial function and inhibiting ER stress. Notably, in *C9ORF72*-ALS human patient-iMNs and directly fibroblast-converted neurons, KMP counteracted mitochondrial deficits and provided neuroprotection in the presence of elevated ER stress, thus indicating the probable translational potential of KMP. Additionally, in vivo, treatment with KMP in the symptomatic rodent model of *C9ORF72*-ALS was successful in reducing pathological hallmarks and concomitantly delaying the progression of behavioral pathology. Lastly, in silico modeling identified a novel prominent binding affinity of KMP to chaperone GRP75 and mechanistically the neuroprotective mechanism of KMP is through the iP3R-VDAC1 pathway via the modulation of GRP75 and ATP5J expression.

Experimental procedures

Mice strains

The *C9-500* BAC mouse line (FVB/NJ-Tg(*C9orf72*)500Lpwr/l) carrying a human *C9ORF72* gene under a human promoter with ~500 hexanucleotide repeats described in (Liu et al., 2016) [27, 28] was purchased from Jackson Laboratory (RRID: IMSR_JAX:029099) and kept in heterozygosis crossed with (non-carrier) mice FVB/NJ (Janvier labs, SC-FVBN-F). Our colony displays an acute phenotype, which is observed in 25–30% of females with a median life span of 105 days whereas the remaining female and male mice exhibit a slow-progressing phenotype with females having a median life span of approximately 250 days and males 260 days. Long-range PCR was regularly done to identify repeat length-matched cohorts. KMP treatment included both genders and only slow-progressing mice. All behavior and survival assays were performed in repeat length-matched (700–800 repeats). Animal care, housing, ethical experimental usage, and procedures were in accordance with the Swiss Veterinary Law guidelines, and the study was approved by the Animal Commission of Canton of Bern, Switzerland, license number BE-35/17, BE-82/18.

In vivo/in vitro drug treatments

KMP (Sigma-Aldrich, K0133) at 10 mg/kg was administered via i.p. injections daily to both wild type (*WT*) and *C9-500* starting at symptomatic age P138 for the first two weeks, followed by every alternate day KMP administration until end-stage P240. *WT* and *C9-500* mice were treated every alternate day with Salubrinal (Sal) (Enzo life sciences, 270-428-M005) at a dosage of 1 mg/Kg or saline starting at symptomatic age P145 until P180. iMNs or dNs were treated with Tunicamycin (TU) (1 µg/ml) for 24 h before further analysis. For KMP treatments, iMNs were treated with 10 µg/ml KMP for 2 h or 48 h.

Reverse rotarod and hanging wire test

Rotarod apparatus (Ugo Basile, Comerio, Italy) was used to assess general motor performance as well as motor coordination and endurance as usually assessed by common accelerated rotarod protocols, during the light phase of the 12 h light/12 h dark cycle. For the inverse rotarod, the protocol involved sequential acceleration (from 15 to 33 rpm in 10 s) and deceleration (from 33 to 15 rpm in 10 s) followed by the immediate inversion of the direction of the rod, and the same rotation protocol was again followed. One trial lasted a maximum of 110 s, with 3 min (min) resting in between trials. Three trials every 10 days were performed for *C9-500* animals and respective controls, while initially, KMP-treated animals were tested for 4 consecutive days. Mice were trained on the rotating rod at a fixed speed for 3 days before the baseline recording. All measurements were done blindly without knowing the genotype of the mice. The hanging wire test was performed as previously described [29]. Briefly: mice were placed on a cage top and once the animal was stable on top of the grid, the cage top was gently inverted, and the latency of the first fall was recorded. All the animals are placed on the inverted cage top each time they fall to assess the average number of falls. The test lasts for 120 s.

iPSC differentiation into motor neurons (iMNs)

The healthy and *C9ORF72*-ALS iPSCs were obtained from iPSC bank (Biomedicum Stem Cell Center, GoEditStem platform, HiLIFE, Helsinki, Finland and the iPSC Core, Cedar Sinai, USA). iPSCs were cultured in Geltrex™ (ThermoFischer) coated plates in mTeSR (StemCell technologies) media. MN differentiation was performed as previously described [30, 31] with some modifications. Human iPSCs were dissociated to single cells using Accutase (StemCell technologies) and seeded at 3X10⁶ onto 10 cm plate with N2B27 differentiation medium (Advanced DMEM/F12:Neurobasal (1:1) medium, 1% Pen/strep (Gibco), 1% GlutaMAX (Gibco), 0.1 mM 2-mercaptoethanol (Gibco), 1X B27 supplement (Gibco), 1X N2 supplement (Gibco), supplemented

with 10 ng/ml basic fibroblast growth factor ((StemCell technologies), 20 µM SB431542 (StemCell technologies), 0.1 µM LDN193189 (StemCell technologies), 3 µM CHIR99021 (StemCell technologies), 10 µM L-Ascorbic Acid (L-AA; Sigma) and 1X Revitacell supplement (Gibco)) to initiate the formation of embryoid bodies (EBs). On day 2 media patterning of EBs was induced by the addition of media supplemented with 100 nM all-trans retinoic acid (RA; sigma) and 500 nM Smoothed Agonist (SAG; StemCell technologies). EBs were pelleted and fed with fresh media on every alternate day until day 14. 10 ng/ml Brain derived neurotrophic factor (BDNF; StemCell technologies) was added from day 7 while 10 µM DAPT (StemCell technologies) was added from day 9. EBs were dissociated using trypsin on day 16 and triturated with ice cold cell trituration and wash medium (1X PBS (Gibco), 0.45% Glucose, 0.1% Bovine Serum Albumin (BSA; Sigma), 2 mM MgCl₂, 0.8 mM EDTA (Invitrogen), 2.5% Fetal Bovine Serum (FBS; Sigma), 1X N2 supplement, 1X B27 supplement and DNase). Triturated EBs were then plated on poly-ornithine/laminin (Sigma) coated plates in MN feeding medium (Neurobasal medium (Gibco), 1X glutaMAX, 1X Non-essential amino acid (NEAA, Gibco), 0.1 mM 2-mercapthoethanol, 1X N2 supplement, 1X Pen/strep, 1X B27 supplement, 10 ng/ml glial cell derived neurotrophic factor (GDNF; StemCell technologies), BDNF 10 ng/ml, 10 ng/ml insulin-like growth factor (IGF-1; StemCell technologies), 10 ng/ml Ciliary neurotrophic factor (CNTF; StemCell technologies), 100 nM RA and 10 µM AA and kept at incubator at 37 °C and 5% CO₂ for further maturation.

Generation of direct fibroblast-induced neurons (dNs)

Fibroblast collection: skin punches were collected, and fibroblasts were grown in fibroblast media (10% FBS (Gibco), 1% anti-anti (Gibco) in DMEM Glutamax (Gibco)) for up to 1 month, passaging once every 1–2 weeks. In addition, this study used a fibroblast sample from the NINDS Repository, as well as clinical data. NINDS Repository sample numbers corresponding to the samples used are: AG08620. Patient skin-derived fibroblasts were directly reprogrammed into neural progenitor cells (NPCs) as previously described [32]. Briefly, 100,000–200,000 fibroblasts were seeded into a fibronectin (5 µg/mL, Millipore) coated 6-well plate and cultured in a 37 °C, 5% CO₂ incubator. The next day, fibroblasts were transduced with retroviruses for SOX2, cMyc, KLF4, and OCT3/4. 24 h later virus was removed, and the media was replaced with fresh fibroblast media (10% FBS (Gibco), 1% anti-anti (Gibco) in DMEM Glutamax (Gibco)). After a 24-h rest period, the media of transduced fibroblasts was changed to a neuralizing media (1% B27 (Gibco), 1% N2 (GIBCO), 1% anti-anti (Gibco),

20 ng/mL FGF2 (peprotech), 20 ng/mL EGF (peprotech), and 5 µg/mL heparin (Sigma)). Cells were cultured in this media until converted into NPC. NPCs were cultured in (1% B27 (Gibco), 1% N2 (Gibco), 1% anti-anti (Gibco), 20 ng/mL FGF2 (peprotech)). Induced direct neuron generation (dNeus): patient and healthy fibroblasts were directly converted to neurons using small molecules as previously described [28]. Briefly, 10 cm plates were coated overnight with polyornithine (10 µg/mL, Sigma) in borate buffer. The next day, plates were washed with DPBS and coated with laminin (5 µg/mL, Invitrogen) and fibronectin (2.5 µg/mL, Millipore Sigma) in DMEM/F12 at 37 °C for 2 h. Fibroblast cells (850,000) were seeded onto the plates in culture medium for 1 day. The cells were transferred to neuronal induction medium (DMEM/F12: Neurobasal (Gibco) [1:1] with 0.5% N-2 (Gibco), 1% B-27 (Gibco), 100 µM cAMP (Sigma), and 20 ng/mL bFGF (Peprotech)) with the following chemicals: VPA (0.5 mM, Sigma), CHIR99021 (3 µM, Axon medchem), repsox (1 µM, BioVision), forskolin (10 µM, Tocris), SP600125 (10 µM, Sigma), GO6983 (5 µM, Sigma) and Y-27632 (5 µM, Sigma). Half the medium was changed after 3 days with a fresh induction medium. On the fifth day, cells were switched to neuronal maturation medium (DMEM/F12: Neurobasal [1:1] with 0.5% N-2 (Gibco), 1% B-27 (Gibco), 100 µM cAMP (Sigma), 20 ng/mL bFGF (Peprotech), 20 ng/mL BDNF (Gibco) and 20 ng/mL GDNF (Gibco)) with the following chemicals: CHIR99021 (3 µM), forskolin (10 µM) and SP600125 (10 µM).

Immunofluorescence on iMNs

iMNs plated on coverslips were fixed using 4% paraformaldehyde (PFA) for 15 min and blocked for 1 h with 3% bovine serum albumin (BSA) and 0.1% TritonX-100 in phosphate-buffered saline PBS. After blocking, neurons were incubated with the following primary antibody: anti-BiP (Abcam, ab21685, 1:500), goat anti-ChAT (Millipore, AB144P, 1:500), chicken anti-MAP2 (Sigma Aldrich, AB15452, 1:500) (Thermo fisher scientific, Invitrogen PA5-29202, 1:500) in blocking buffer overnight at 4 °C. After washing three times with PBS, cells were incubated in a blocking buffer with Alexa Fluor fluorescently labeled secondary antibodies and DAPI for 1 h at room temperature. Cells were then washed with PBS and mounted on glass slides. Images were acquired with a confocal microscope Olympus FluoView™ FV1000 (Olympus) fitted with a 20X or 40×air objective and 60×immersion oil objective.

Immunofluorescence and immunohistochemistry of rodent tissue

Mice were transcardially perfused with 4% PFA in 1X PBS; brain, cerebellum and lumbar spinal cord were isolated and kept overnight at 4 °C in the same fixative solution, followed by 30% sucrose in PBS for cryoprotection until samples were used. After embedding in Tissue Tek O.C.T compound (Bio system, 4583). Spinal cord (50 µm), sections were cut using a cryostat. Antibodies used for immunofluorescence were: rabbit anti-GRP78/BiP (1:500, Abcam, ab21685), mouse anti-KDEL/BiP (1:500, Enzo Life Science, SPA-827), rabbit anti-P_i-EIF2α (1:25, Cell Signaling, 3597L), goat-anti ChAT (1:1000, Millipore, AB144P), mouse anti-GRP75 (1:200, Abcam, ab2799), rabbit anti-GRP75 (1:200, Abcam, ab53098), rabbit anti-GFAP (1:500, Abcam, ab7260), mouse anti-8-hydroxyguanosine (8-OHdG), (1:500, Abcam, ab62623) mouse anti-NeuN clone 60 (1:1000, Millipore, MAB377). Heat-mediated antigen retrieval was performed using Sodium citrate buffer 10 mM pH 6 for GRP75 and ATP5J staining. Sections were kept for 2 h in PBS solution containing 0.05% Triton X-100 and 10% normal donkey serum (NDS, Jackson immunoresearch, 017-000-121) after the antibodies were applied in PBS, 3% normal donkey serum (NDS), 0.05% Triton X-100, and incubated overnight (for brain) and for two days for the spinal cord at 4 °C. Sections were then briefly washed with PBS and incubated for 120 min at room temperature, with appropriate combinations of secondary antibodies from Invitrogen.

Spinal cord sections for immunohistochemistry were processed as follows: sections were treated with heat-mediated antigen retrieval using sodium citrate buffer 10 mM pH 6 and immersed in 3% H₂O₂ in PBS for 20 min to block endogenous peroxidase activity. This was followed by a blocking step in PBS containing 0.05% Triton X-100 and 10% NDS and incubated overnight at 4 °C with goat anti-ChAT (1:500, Millipore, AB144P) antibody diluted in the same blocking solution. The next day the sections were incubated with the appropriate biotinylated secondary antibody (1:500) followed by 1 h incubation in PBS solution containing biotin-avidin complex (1:100, Vector Labs), finally, the 3,3'-diaminobenzidine (DAB) reaction was developed. The glass slides were dehydrated via ascending concentrations of ethanol and rinsed in xylene before adding the coverslip. Images were acquired using an Olympus microscope (BX51).

Muscles histology

Mice were deeply anesthetized with isoflurane and decapitated before the gastrocnemius muscles were dissected. Muscles were quickly frozen in liquid nitrogen-cooled isopentane. 8 µm thick sections were cut on a cryostat and placed directly onto coverslips. For

hematoxylin & eosin (H&E) staining, muscle sections were stained with Mayers hematoxylin for 5 min, followed by three 10 min washes in deionized H₂O. Muscles were then placed in eosin G for 1 min and then rinsed in 70% ethanol. The tissue was then dehydrated in a series of ethanol washes (70%, 95%, 100%), rinsed in xylene, and then mounted on a glass slide. NADH staining was performed by incubating muscle sections in 0.2 M Tris buffer containing Nitroretetrazolium Blue (Sigma) and β -nicotinamide adenine dinucleotide (NADH, Sigma) for 30 min at 37 °C. Following three washes in deionized H₂O, coverslips were mounted onto a glass slide. ATP staining pH 4.3 and 9.4 were performed by incubating the slides in pre-incubating solution pH4.3 per 10 min at 4°, containing 0.1 M Na acetate buffer with 10 mM EDTA. Followed by three 5 min washes in deionized H₂O, to be then incubated in the incubation solution: for pH 4.3 containing sodium acetate 0.1 M, EDTA 0.1 M pH8 and pH 9.4 containing 0.1 M glycine (Sigma, 50,046), 5 mg ATP and DTT in NaCl buffer with CaCl₂ per 30 min at 37 °C. Coverslips were then washed with deionized H₂O 3 times every 5 min, incubated with Cobalt chloride 2% 3 times per 1 min at room temperature, rinsed with deionized water, and incubated with ammonium sulfide 1% at room temperature for 30 s. Coverslips were rinsed under running water, dehydrated in a series of ethanol washes (70%, 95%, 100%), rinsed in xylene, and then mounted on a glass slide.

Imaging and image analysis

Confocal images were acquired using a Leica SP5 (Leica Microsystems) fitted with a 20X, 40 and 63X oil objective, Leica SP8 (Leica Microsystems) fitted with a 63X oil objective, or Olympus Fluoview 1000-BX61 (Olympus, Tokyo) microscope, fitted with a 20X, 40X air objective or 60X immersion oil objective. All images were processed using Imaris software version 7.6.3 or Fiji. For the analysis of BiP, P_i-EIF2 α , GRP75, GFAP, 8-OHdG and ATP5J labeling intensities, data were acquired using identical confocal settings, with signals at the brightest cells being non-saturated, and background levels outside MN pools were still detectable. Images were analyzed quantitatively using Fiji or Imaris. Signal intensity values for the antigen of interest were calculated over several consecutive lumbar spinal cord Z-stack spaced 0.5 μ m, after background subtraction from every different channel. For the calculation of MN percentages, Choline Acetyltransferase (ChAT) positive MNs were examined and signal intensity values for the antigen of interest within these ChAT positive MNs were calculated in 3–4 animals. Lowest signals had values of below 50 and high-intensity neurons exhibited labeling values up to 255. Signal values below 50 in the case of BiP in *WT* animals were counted

as basal expression. To count MN numbers, a cell counter plugin from Fiji was used. Imaris software was used to reconstruct the 3D isosurface of Poly(GA) aggregates volume.

Proximity ligation assay (PLA) in perfused mouse spinal cord tissue

PLA was adapted from Gomes et al., [33]. In short, 50 μ m free-floating spinal cord sections were mounted on a frost slide (Huberlab, 10.0120.04) and air-dried. Slides were rinsed in 0.01% Triton X-100 in 1X PBS per 12 min followed by 3 washes in 1X PBS (each wash was for 5 min). Slides were kept in a humid chamber and blocking solution was added (Duolink PLA probe kit, DUO92008, Merck) for 1 h at 37 °C. Subsequently, slides were incubated with the following primary antibodies (1:200, rabbit anti-IP3R, ABCAM, ab5804; 1:100, mouse anti-GRP75, ABCAM, ab53098; 1:100, rabbit anti-GRP75, ABCAM, ab227215; 1:200 rabbit anti-ATP5J, Thermo Fisher Scientific, PA5-29202) in a humidity chamber for 2 nights at 4 °C. Slides were rinsed in buffer A (Duolink In Situ Wash Buffers, Fluorescence DUO82049) (3 times every 5 min) and incubated with PLA probes (Probe Anti-mouse MINUS, DUO92004 and Probe anti-rabbit PLUS, DUO92002) at a working concentration of 1:10 for 1 h at 37 °C. Ligation (Duolink In Situ Detection Reagents Red, DUO92008) was performed at 37 °C per 45 min followed by 3 washes in buffer A (3 per 5 min). The amplification (Duolink In Situ Detection Reagents Red, DUO92008) step was performed at 37 °C in a dark humidity chamber for 100 min. Finally, sections were rinsed in buffer B (Duolink In Situ Wash Buffers, Fluorescence DUO82049) (2 per 10 min) followed by a third wash in 0.001% buffer B. Slides were left to dry and coverslips were mounted with Duolink In Situ Mounting Medium with DAPI (DUO82040), and edges were sealed with nail polish. Sections were kept at -20 overnight before confocal imaging.

Colorimetric staining of mitochondria complexes

Mice were rapidly perfused with PBS, fresh spinal cord was removed, embedded in O.C.T compound, and quickly frozen on dry ice. 20 μ m thick sections were cut with a cryostat and transferred onto an adhesive glass slide. Sections were incubated for 30 min at 37 °C in freshly prepared appropriate complex histochemistry media: (1) Complex I: 1.23 mg/ml (1.5 mM) Nitroblue tetrazolium (NBT; N6876, Sigma) and 0.625 mg/ml NADH (N8129, Sigma) were mixed in PBS, pH=7.4. Complex IV: 0.5 mg/ml 3,3'-diaminobenzidine tetrahydrochloride (DAB, D7304, Sigma), 1 mg/ml cytochrome c (C2506, Sigma), and approximately 2 μ g/ml (a few crystals) bovine catalase (C9322, Sigma) were mixed in

PBS, pH 7.4. After the staining of each complex, sections were washed 3×10 min in PBS before being dehydrated for 4 min in 70% ETOH, 4 min in 90% ETOH, 10 min in 100% ETOH, and 10 min in Xylol, and mounted with Eukitt. Images were acquired using an Olympus microscope (BX51).

Mitochondrial calcium imaging

Mitochondrial Ca²⁺ imaging for cortical neurons was adapted from [34]. In brief, cells were incubated for 45 min with the staining solution containing: 156 mM NaCl, 3 mM KCl, 2 mM MgSO₄, 1.25 mM KH₂PO₄, 10 mM D-glucose, 2 mM CaCl₂, and 10 mM HEPES pH 7.35, 5 µg/ml (w/v) Fluo-4, AM, 10 µM Verapamil. After a brief wash with Ca²⁺ free HBSS, cells were incubated for 10 min with the intracellular solution containing: 6 mM NaCl, 130 mM KCl, 7.8 mM MgCl₂, 1 mM KH₂PO₄, 0.4 mM CaCl₂, 2 mM EGTA, 10 mM HEDTA, 2 mM malate, 2 mM glutamate, 2 mM ADP, 20 mM HEPES pH 7.1, 25 µg/ml (w/v) digitonin and 1 µM thapsigargin. An Olympus Fluoview 1000-BX61 (Olympus, Tokyo) microscope fitted with a 40× water immersion objective was used to acquire images every 20 s, the first 60 s were considered as the baseline, afterward 50 mM KCl was added to the imaging solution to depolarize the cells. Neurons

were treated with 10 µg/ml of KMP for 1 h before staining solution passage, moreover, to maintain their effect the KMP was also added to the staining solution before starting the imaging for a total time of treatment of 1 h and 45 min. Images were analyzed using Fiji, multiple regions of interest (ROI) were chosen inside the cytosol of the cells and the fluorescence intensity was calculated over the different frames. To calculate ΔF, the median intensity values are divided by the average of the first 60 s of recording (F0) per ROI.

CB-Dock analyses and PharmaMapper

CB-Dock is a computational docking tool specifically designed for molecular docking tasks, focusing on the flexible docking of small molecules into protein binding sites. CB-Dock uses a cavity-detection algorithm to identify potential binding pockets on a protein's surface, eliminating the need for manually specifying binding sites. Its name is derived from "cavity-based docking," for automatically identifying and targeting protein binding sites. The receptor (GRP75) protein structure was downloaded from the Protein Data Bank (PDB) and the ligand KMP or 17-AAG representing the small molecule intended for docking was downloaded in MOL2 format. Both files

Table 1 Description of the human iPSC lines used in the study: demographic information about iPSC and fibroblast lines from C9ORF72-ALS/FTD patients and healthy control (CTRL) employed to generate iMNs and dNs

Subject	Mutation	Age	Sex	Race/nationality	ALSFRS-R score at screen	Onset till biopsy	Notes
Control 1	Healthy	30	M	Asian	N/A	N/A	
Control 2	Healthy		M				Commercially available System Bioscience Cat. SC950A-1
Control 3	Healthy		F	Caucasian			Pilotto et al. <i>Acta Neuropathologica</i> 144, 939–966 (2022)
C9ORF72 1	C9ORF72 positive		M	Caucasian			Donnelly, C.J. et al. <i>Neuron</i> 80,415–428 (2013)
C9ORF72 2	C9ORF72 positive		M	Caucasian			Donnelly, C.J. et al. <i>Neuron</i> 80,415–428 (2013)
C9ORF72 3 and its isogenic line	C9ORF72 positive	38	F	Dutch		1 year	Mehta, A.R. et al. <i>Acta Neuropathologica</i> 141, 257–279 (2021)
C9ORF72 4	C9ORF72 positive	52	M	Caucasian			Pilotto et al. <i>Acta Neuropathologica</i> 144, 939–966 (2022)
C9ORF725	C9ORF72 positive	51	M	Caucasian		< 1 year	Pilotto et al. <i>Acta Neuropathologica</i> 144, 939–966 (2022)
C9ORF726	C9ORF72 positive	67	F	Caucasian			Pilotto et al. <i>Acta Neuropathologica</i> 144, 939–966 (2022)

were uploaded on the CB-Dock platform, where the cavity-detection algorithm identified binding sites (pockets) on the protein structure. These pockets are ranked based on size and accessibility, and the software optimizes the ligand's conformation within the binding site to achieve the best fit and a Vina score is given. The Vina score is a numerical value generated by AutoDock Vina, and the score is expressed in kcal/mol and reflects the estimated free energy of binding. A more negative Vina score indicates stronger predicted binding affinity, meaning the ligand is more likely to bind tightly to the receptor. PharmaMapper was used to identify potential protein targets for a given small molecule; KMP and 17-AAG by comparing the molecule's structure against a large database of 3D pharmacophore models derived from known protein structures.

Statistical analysis

Statistical significances throughout the paper were evaluated by two-tailed, paired, and unpaired Student's t test and one or two-way ANOVA. Post ANOVA Bonferroni, Sidak, and Tukey's test were used to evaluate statistical significance throughout the paper as indicated in the respective figure legend. Values are expressed as mean \pm standard error of the mean (SEM). Error bars: SEM * $P < 0.05$, ** $P < 0.01$, *** $P < 0.001$.

Results

Kaempferol protects human iMNs and fibroblast-induced neurons (dNs)

We started the study by evaluating the neuroprotective action of KMP, a compound known to act on UPR

and oxidative stress pathways. Firstly, we generated human *C9ORF72* iMNs as previously described [7]. iPSCs from two healthy controls, three *C9ORF72* lines, and one isogenic control were differentiated into iMNs, see (Table 1) for demographic details and (Suppl. Figure 1) for iMN molecular characterization. Since Ca^{2+} homeostasis is a crucial determinant for neuronal function, and Ca^{2+} buffering by mitochondria majorly occurs at the ER-mitochondria contact sites, which is important for ATP production, we first employed the seahorse assay to measure mitochondrial function. Seahorse assay measures key parameters of mitochondrial function by directly measuring the oxygen consumption rate (OCR) and a representative example from control and diseased *C9ORF72* line, C9(1) is presented pre- and post-KMP treatment (Fig. 1A). Notably, all three *C9ORF72* patient-derived iMNs revealed impaired mitochondrial function as observed by the reduced basal respiration and ATP production compared to the healthy control treatment of iMNs with KMP for 48 h rescued mitochondrial dysfunction by normalizing basal respiration (Fig. 1B) and ATP levels (Fig. 1C). Note the near normalized ATP levels in mutation-corrected *Iso-C9* (3) patient line, compared to the uncorrected *C9* (3) patient line, suggesting that the observed mitochondrial dysfunction is causally linked to the disease mutation. Next, we tested whether KMP would protect mutant iMNs from ER stress and thus sustain neuroprotection. To this end, we induced strong ER stress by treating iMNs with tunicamycin (TU) for 24 h. In parallel, iMNs were dually treated with TU and KMP for 24 h (scheme Fig. 1D). TU treatment led to the induction of ER stress as observed by increased BiP expression in both *control* and *C9ORF72* patient-derived

(See figure on next page.)

Fig. 1 KMP restores mitochondria impairments and inhibits ER stress in *C9ORF72* neurons. **a** Seahorse graph plotted for oxygen consumption rate (OCR) on y-axis with time on X-axis. Representative traces of mitochondrial respiration from *Ctrl*(1) and *C9*(1) iMNs, showing mitochondrial functional deficits in *C9ORF72* patient line at one week, but those deficits are normalized after KMP treatment. **b** Mitochondrial oxygen consumption rate analysis on iMNs reveals impairments in basal respiration in all three *C9ORF72* patient lines compared to healthy control or respective isogenic control. Basal respiration is restored to control level after KMP treatment (Unpaired t-test: *CNTRL* (1) vs *C9* (1) ***; *CNTRL* (1) vs *C9* (1) + KMP n.s.; *CNTRL* (2) vs *C9* (2) ***; *CNTRL* (2) vs *C9* (2) + KMP n.s.; *Iso-C9* (3) vs *C9* (3) *; *Iso-C9* (3) vs *C9* (3) + KMP *). The experiment was performed in triplicates from three different batches of iPSC conversion to iMNs. **c** Mitochondria OCR analysis on iMNs reveals impairments in ATP production in all *C9ORF72* patient lines compared to healthy control or respective isogenic. ATP production is restored to the control level after KMP treatment (Unpaired t-test: *CNTRL* (1) vs *C9* (1) **; *CNTRL* (1) vs *C9* (1) + KMP * *CNTRL* (2) vs *C9* (2) ***; *CNTRL* (2) vs *C9* (2) + KMP *; *Iso-C9* (3) vs *C9* (3) *; *Iso-C9* (3) vs *C9* (3) + KMP n.s.). Experiment was performed in triplicates from three iPSC batches converted to iMNs. **d** Schematic depiction of the experimental timeline for iMNs TU treatment and TU treatment combined with 24 h of KMP. **e** Representative confocal images of BiP immunostaining in iMNs, quantitative analysis revealed an increase in BiP expression after 24 h TU treatment, whereas ER stress was completely inhibited after TU + KMP treatment. (Unpaired t-test: *CNTRL* (1–2) vs *C9* (1,2) n.s. *Iso-C9* (3) vs *C9* (3) n.s.; *CNTRL* (1–2) vs *CNTRL* (1–2) + TU***; *C9* (1–2) vs *C9* (1–2) + TU***; *Iso-C9* (3) vs *Iso-C9* (3) + TU ***; *C9* (3) vs *C9* (3) + TU ***; *CNTRL* (1–2) + TU vs *CNTRL* (1–2) + TU + KMP ***; *C9* (1–2) + TU vs *C9* (1–2) + TU + KMP***; *Iso-C9* (3) + TU vs *Iso-C9* (3) + TU + KMP ***; *C9* (3) + TU vs *C9* (3) + TU + KMP***). Scale bars: 100 μ m. **f** *CNTRL* and *C9* iMNs treated with TU displayed significant cell death, whereas the addition of KMP for 24 h was found to be neuroprotective (TU: *CNTRL* (1) 41% alive vs 59% dead; *C9* (1) 45% alive vs 55% dead; *C9* (2) 35% alive vs 65% dead; TU + KMP: *CNTRL* (1) 96% alive vs 4% dead; *C9* (1) 93% alive vs 7% dead; *C9* (2) 81% alive vs 19% dead). Scale bars: 10 μ m. **g** Schematic depiction of the experimental timeline for dNs generation, TU treatment and TU treatment combined with 24 h of KMP. **h** *CNTRL* and *C9* dNs treated with TU displayed significant cell death, whereas those treated with KMP for 24 h were resilient to ER stress-induced neurodegeneration

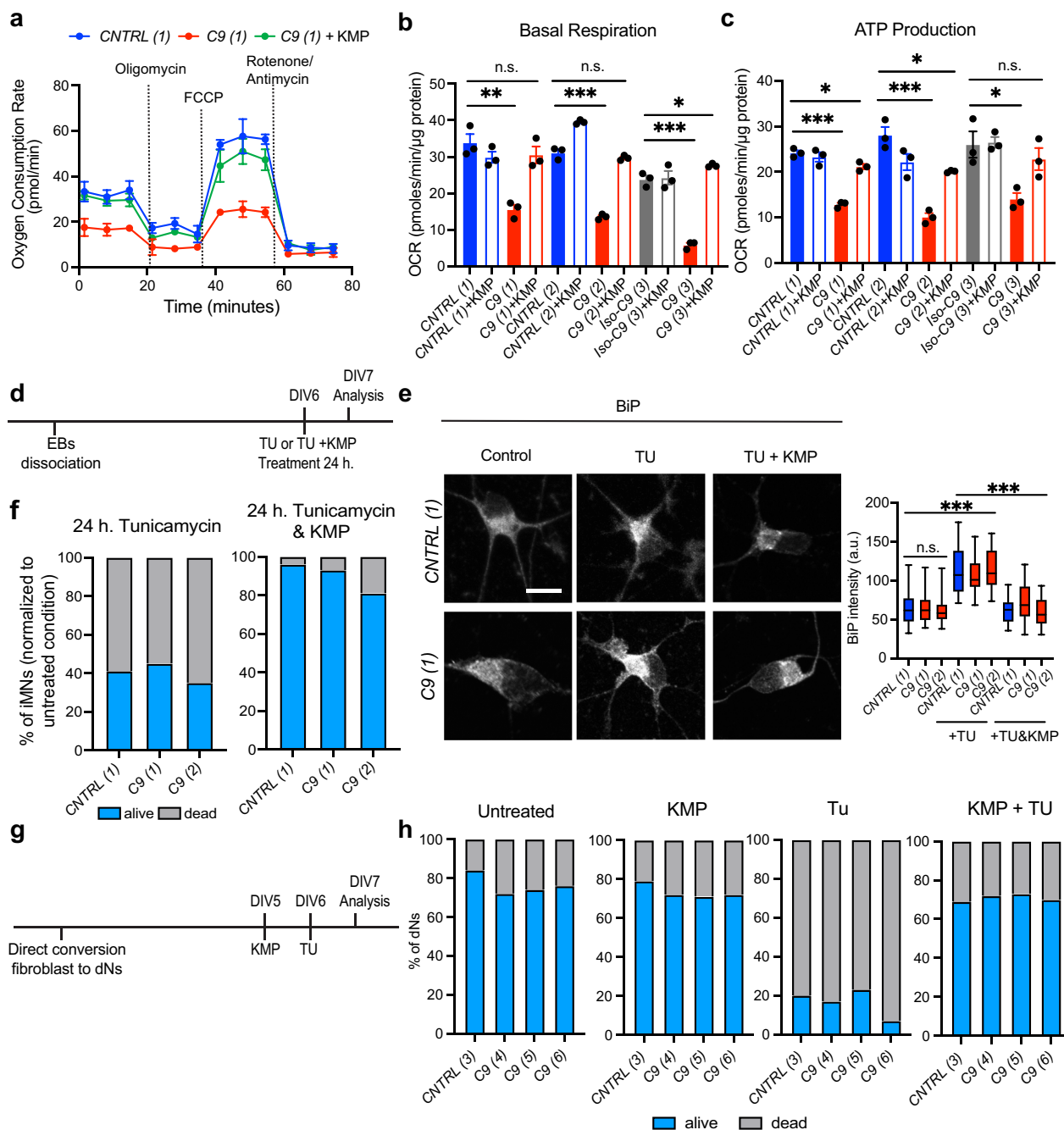


Fig. 1 (See legend on previous page.)

iMNs. Notably, dual treatment with TU and KMP for 24 h inhibited the observed ER stress response, indicating that KMP even in the presence of ER stress activators can effectively counteract the onset of ER stress (Fig. 1E). We next examined whether KMP treatment could protect iMNs from degeneration due to ER stress. TU treatment for 24 h led to a substantial loss of iMNs with nearly 60% of iMNs being dead in both control and

diseased conditions. In contrast, dually treated iMNs exhibited negligible neuronal death, indicating that KMP can confer neuroprotection in conditions associated with strong ER stress (Fig. 1F). Given the prominent role of aging in neurodegeneration, we next generated neurons via the direct reprogramming of fibroblasts to neurons (dNs), as previously described by us [7], thus maintaining the aging and epigenetic signatures of the donor. See

(Table 1) for demographic details. We treated dNs either with TU for 24 h or KMP for 48 h, followed for the last 24 h of culture with co-treatment with TU (scheme Fig. 1G), which was similar to our experiments in iMNs led to significant death in controls and *C9ORF72* dNs, however, the dual treatment together with KMP counteracted ER-stress induced neuronal death irrespective of their genotype (Fig. 1H). In conclusion, KMP treatment restores mitochondrial function, and provides neuroprotection against ER stress, thereby alleviating cellular dysfunction in human *C9ORF72*-patient neurons.

Kaempferol treatment protects MNs and reduces pathological aggregates in a rodent model

Next, we determined whether KMP treatment exerted a neuroprotective effect on MNs in the *C9-500* model of *C9ORF72*-ALS. This mouse model displays premature ER stress, mitochondrial dysfunction as well as the striking presence of RNA foci, pTDP43 aggregates, and robust accumulation of DPRs, all of which are pathological hallmarks of *C9ORF72*-ALS [7, 35–37]. We performed chronic KMP treatment from P138 until P240, an age-corresponding to the end stage of the disease [29, 35]. Firstly, counting the number of ChAT immunostained spinal MNs revealed that the number of MNs was substantially higher in *C9-500* mice treated with KMP than in saline-treated, control mice. Notably, the treatment led to a comparable number of mutant MNs as those observed in *WT* mice, suggestive of sustained neuroprotection. In comparison, a ~40% reduction in MN numbers, indicative of ongoing MN degeneration, was observed in the spinal cord of saline-injected mice (Fig. 2A). Poly(GA) inclusions are prominent pathological hallmarks, indicative of progressing disease and their expression is dependent on P_1 -eIF2 α signaling, which is induced during unfolded protein response (UPR) and/or

integrated stress response (ISR) [38–40]. We longitudinally assessed from the presymptomatic stage (P60) until the symptomatic stage (P150), the presence of Poly(GA) inclusion within spinal MNs of *C9-500* mice. Immunostaining against N-terminal Poly(GA), revealed that $15.1 \pm 3.4\%$ of Poly(GA) aggregates were $>1 \mu\text{m}^3$ at P60, however, this fraction of the larger Poly(GA) aggregates increased with age, coinciding with the symptomatic phase ($32.9 \pm 2.8\% >1 \mu\text{m}^3$ at P125, and $50.8 \pm 2.1\% >1 \mu\text{m}^3$ at P150). Note the complete lack of Poly(GA) immunopositivity in *WT* MNs (Fig. 2B, graph bottom). Since sustained MN numbers after KMP treatment indicated a neuroprotective action of KMP, thus we examined the accumulation of Poly(GA) aggregates within MNs as an indicator of improved neuronal homeostasis. Immunostaining against Poly(GA) and quantification revealed widespread accumulation of Poly(GA) inclusions within saline-treated *C9-500* spinal MNs, however, the average numbers, as well as the fraction of large Poly(GA) aggregates within individual MNs, were dramatically reduced within chronically KMP treated *C9-500* mice (Fig. 2C). Astroglialosis is a typical hallmark of many neurodegenerative diseases as well as ALS, thus we stained lumbar spinal cord sections for the glial fibrillary acidic protein (GFAP), to assess if KMP has an effect in reducing neuroinflammatory events. While *C9-500* control animals show widespread astroglialosis within the ventral horn of the spinal cord, KMP-treated *C9-500* mice display a reduction in GFAP intensity (Fig. 2D). As *C9ORF72*-linked ALS also affects the muscles, mainly the neuromuscular junctions, we also assessed the overall muscle structure. Muscle histopathological analyses via H&E staining of saline and KMP-treated *C9-500* mice revealed the presence of atrophic fibers, small fiber size, with central nuclei and angular muscle fibers, indicative of muscle fiber deficits and denervation in P240 *C9-500* saline-treated muscle

(See figure on next page.)

Fig. 2 Kaempferol promotes motor neuron survival and reduces pathology progression. **a** Immunohistochemical staining for MN marker ChAT and quantitative analyses. reveals significant differences in motor neuron numbers between *C9-500* mice treated with KMP until the end stage of the disease at P240 and the saline group (Unpaired t-test: *C9-500*+ saline mean \pm SEM 21.75 ± 1.097 vs *C9-500*+ KMP mean \pm SEM 32.48 ± 1.127 , $t=6.455$, $P<0.0001$). Scale bar = 150 μm . **b** ChAT-positive *C9-500* MNs from *C9-500* mice show in an age-dependent manner the accumulation of greater than $1 \mu\text{m}^3$ poly-GA aggregates. (MN numbers: P60 *C9-500*: $n=42$; P125 *C9-500*: $n=47$; P150 *C9-500*: $n=38$; from 4 mice/genotype/age). Scale bar: 30 μm . **c** Quantitative analyses of Poly(GA) aggregates reveal a significant reduction in the number of aggregates in *C9-500* mice treated with KMP (Unpaired t-test: *C9-500*+ saline: $n=19$ MNs vs *C9-500*+ KMP; $n=22$ MNs, $t=3.110$, $P=0.0035^{**}$). Quantitative analysis of PolyGA aggregate volume reveals a significant decrease in $>1 \mu\text{m}^3$ aggregates within spinal MN after KMP treatment (Unpaired t-test: *C9-500*+ saline: $n=19$ MNs vs *C9-500*+ KMP; $n=22$ MNs, $t=3.632$, $P=0.0011^{**}$). $n=4-5$ mice/genotype/treatment. Scale bar: 10 μm . **d** Representative confocal images of GFAP staining and quantitative analysis. Note the reduced astroglialosis in *C9-500* animals treated with KMP (Unpaired t-test: *C9-500*+ saline vs *C9-500*+ KMP ($t=5.789$, $P<0.0001^{***}$)). **e** Representative images of muscle sections with staining for H&E from *C9-500* mice treated with saline and KMP. Blue arrowheads in the H&E images point to small, and degenerating fibers that are not present in *C9-500* mice treated with KMP. Scale bar: 100 μm . **f** Representative images of muscle sections with staining NADH from *C9-500* mice treated with saline and KMP. Red arrows in the NADH staining point to small and degenerating fibers that are not present in *C9-500* mice treated with KMP. Moreover, the NADH staining presents pale fibres in *C9-500* saline animals while in KMP-treated *C9-500* mice, a strong checkboard pattern is present. Scale bar: 150 μm

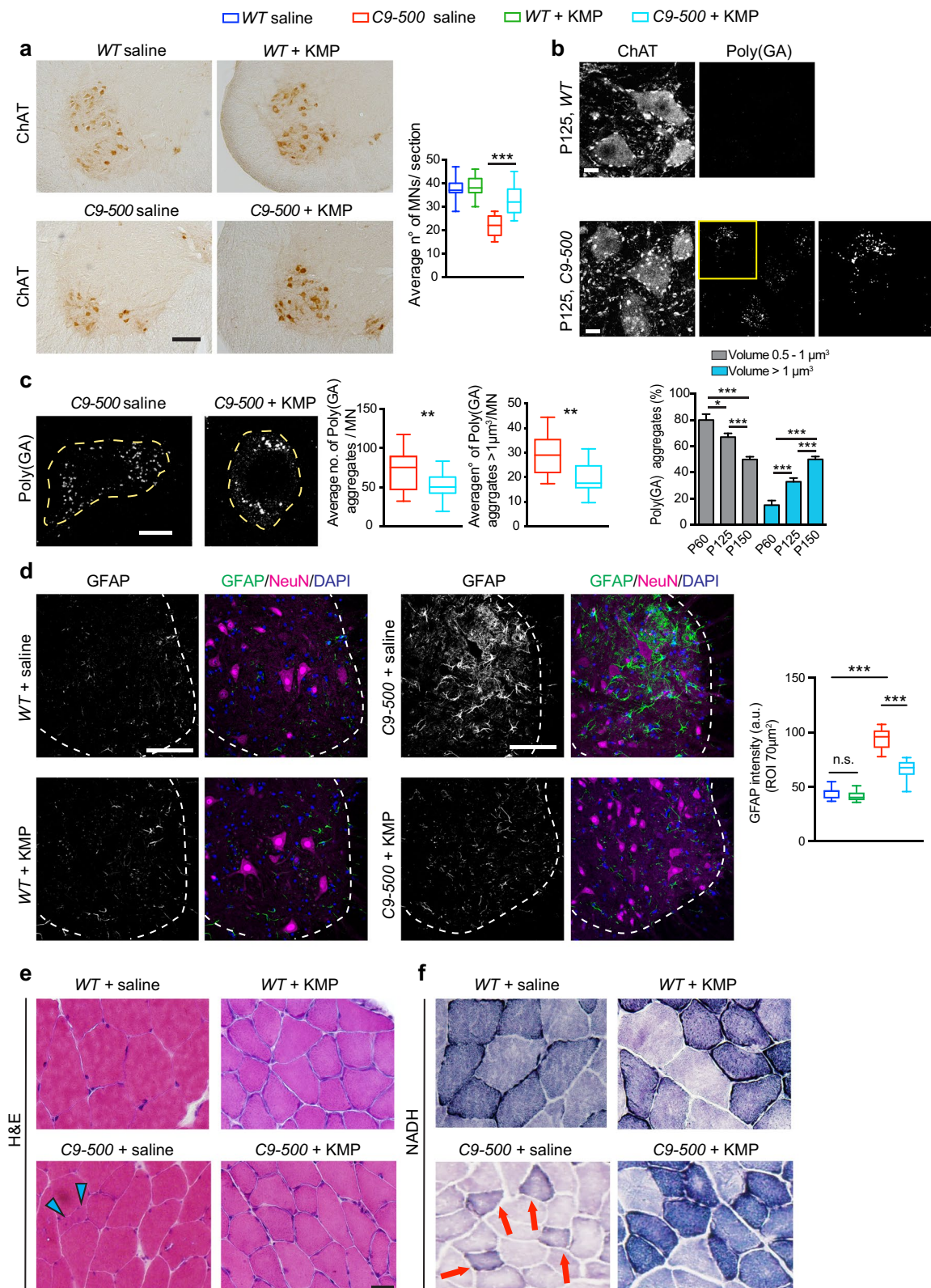


Fig. 2 (See legend on previous page.)

gastrocnemius (GC) muscle. In contrast, KMP-treated mice displayed regular GC muscle fiber size and negligible signs of atrophy (Fig. 2E). Moreover, we evaluated muscle fiber types via NADH staining, which revealed that *C9-500* muscles had nearly lost groups of all NADH-positive myocytes, indicative of muscle deficits. In contrast, KMP-treated mutant *C9-500* muscles maintained a strong NADH staining within groups of myocytes reflecting the presence of varied fiber types and sustained muscle fiber composition in treated *C9-500* mice (Fig. 2F). Overall, this data suggests that the systemic administration of KMP can elicit a beneficial and neuroprotective effect on both spinal cord and muscles as observed by the reduced accumulation of toxic Poly(GA) aggregates, and preserved MN numbers and reduce muscle fiber deficits.

Kaempferol acts on the ER stress pathway and inhibits UPR signaling in vivo

Based on the very promising neuroprotective findings observed after KMP treatment in *C9-500* mice, we next focused on its mode of action on specific cellular impairments. We tested whether KMP, known to possess ER stress inhibitory activity in cultured mammalian cells [17] could also reduce ER stress in vivo in the *C9-500* mouse model. The early phase of ER stress was assessed by immunolabeling the *C9-500* mouse spinal cord sections with antibodies against the luminal ER protein BiP/GRP78. Age-related longitudinal quantification of BiP expression revealed that at P30, *C9-500* MNs expressed similar levels of BiP as in *WT*; but as from P60 on, a gradual increase in BiP expression in mutant MNs was observed. P80 onward, significantly high BiP levels, indicative of ER stress progression was observed (Fig. 3A). We

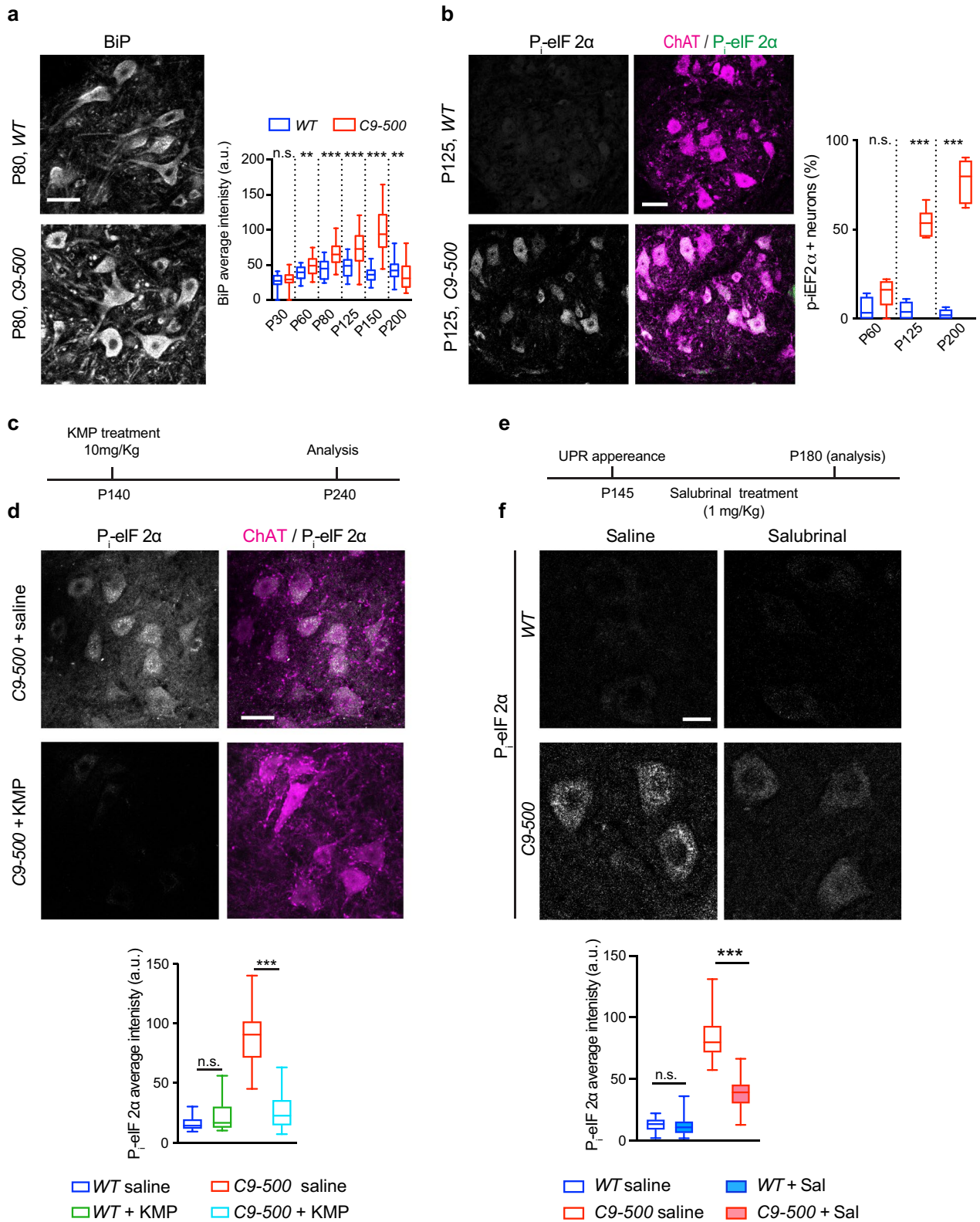
further assessed whether ER stress evolved into UPR by measuring the appearance of P_i -eIF2 α immunoreactivity in ChAT-positive ventral horn MNs. At P60, when BiP levels slightly increased, we found no indication of UPR signaling, however, an abrupt transition to UPR signaling was observed at P125, whereby nearly 50% of MNs displayed strong P_i -eIF2 α immunolabeling ($53.8 \pm 3.8\%$), and nearly all MNs displayed P_i -eIF2 α immunopositivity close to end-stage at P200 ($75 \pm 4.9\%$), confirming an advanced UPR signaling in the majority of *C9-500* MNs (Fig. 3B). Note the complete lack of P_i -eIF2 α immunolabeling within *WT* MNs. Next, we assessed ER stress status in *WT* and *C9-500* mice, which were injected with 10 mg/kg of KMP, which was again started at P138, a timepoint after the onset of UPR signaling and lasted until late end-stage; P240 (scheme for treatment and analyses Fig. 3C). Probing for UPR marker P_i -eIF2 α , we found a prominent expression within mutant *C9-500* MNs at P240, which was restricted to ChAT-positive spinal ventral horn MNs in mutant condition. However, KMP treatment completely inhibited the expression of P_i -eIF2 α indicating that KMP acts on the UPR signaling pathway (Fig. 3D). We next assessed the effect of ER stress inhibitor; Sal on *C9-500* spinal MNs [41]. Chronic treatment with Sal as expected also reduced UPR signaling as observed by diminished P_i -eIF2 α immunopositivity with P180 *C9-500* MNs (Fig. 3E).

Kaempferol restores mitochondria electron transport chain function in *C9-500* mice

Besides ER stress, mitochondrial dysfunction due to *C9ORF72* haploinsufficiency as well as the expression of specific DPRs such as PolyGR [6, 7, 12, 42] has been

(See figure on next page.)

Fig. 3 *C9-500* MNs exhibit early and progressive ER stress and UPR signaling, which is attenuated by kaempferol treatment. **a** Representative images immunolabeled for ER stress marker BiP in *WT* and *C9-500* spinal cord, reveals an increase in BiP intensity within ChAT-positive mutant MNs at P80. The graph on the right depicts quantitative analyses of BiP expression, showing an age-dependent increase within *C9-500* motor neurons as measured in arbitrary units (a.u.). (Unpaired t-test, motor neuron numbers: at P30 *WT*, n = 18 vs *C9-500*, n = 18, t = 0.6159, df = 34 n.s. P = 0.5421; at P60 *WT*, n = 29 vs *C9-500*, n = 28, t = 3.353, df = 55 ***P = 0.0015; at P80 *WT*, n = 27 vs *C9-500*, n = 38, t = 5.741, df = 63, ***P < 0.0001; at P125 *WT*, n = 21 vs *C9-500*, n = 39, t = 4.804, df = 58 ***P < 0.0001; at P150 *WT*, n = 41 vs *C9-500*, n = 53, t = 12.74, df = 92, ***P < 0.0001; at P200 *WT*, n = 58 vs *C9-500*, n = 57, t = 27.11, df = 113, ***P = 0.0078). Scale bar = 30 μ m, n = 4–5 mice/genotype/age. **b** Representative images depicting the appearance of UPR signaling in *C9-500* MNs as measured by the presence of phosphorylated eIF2 α (P_i -eIF2 α) from P125, which encompasses $78\% \pm 3.403$ MNs by P200. Number of ChAT+ve motor neurons analysed at P60 *WT*, n = 85 & *C9-500*, n = 94, at P125 *WT*, n = 82 & *C9-500*, n = 91, at P200 *WT*, n = 192 & *C9-500*, n = 151). Scale bar = 20 μ m, n = 3 mice/genotype/age. **c** Schematic depiction of the experimental timeline for in vivo treatment of symptomatic *C9-500* mice with kaempferol (KMP) until the end stage of disease P240. Initial short treatment lasting for two weeks was performed by daily intraperitoneal (i.p.) injection of kaempferol, followed by injection every alternate day up to P240. **d** Representative images showing the activation of UPR via the expression of P_i -eIF2 α between saline-treated and KMP-treated *C9-500* mice. Quantitative analyses of P_i -eIF2 α expression reveal a significant reduction in UPR levels in *C9-500* MNs after KMP treatment compared to saline controls. One-way ANOVA: P < 0.0001*** F = 48.47, Sidak's multiple comparisons: *WT* + saline vs *WT* + KMP n.s. *C9-500* + saline vs *C9-500* + KMP***. Scale bar = 30 μ m. **e** Scheme showing Sal training schedule. Representative images of P_i -eIF2 α from saline and Sal-treated *WT* and *C9-500* animals. **f** Representative images showing the activation of UPR via the expression of P_i -eIF2 α between saline-treated and ER stress inhibitor Sal-treated *C9-500* mice. Quantitative analyses show reduced expression of P_i -eIF2 α . (One-way ANOVA, F = 306.6, P < 0.0001, Sidak's multiple comparison test: *WT* vs *WT* + Sal, n.s.; *C9-500* vs *C9-500* + Sal,***). Scale bar = 20 μ m, n = 3 animals per genotype/group



causally implicated in *C9ORF72*-linked ALS pathology. Thus, we assessed whether KMP treatment could rescue the observed mitochondrial dysfunction, which has been shown to protect neuronal mitochondria from loss of mitochondrial transmembrane electric potential caused by oxidative stress as well as excessive mitochondrial fission in neuronal models of excitotoxicity and ischemic stroke [43, 44]. We initially evaluated oxidative stress in spinal MNs, given its role in inducing nuclear and mitochondrial DNA damage. This assessment was performed using the oxidative DNA damage marker, 8-hydroxy-2'-deoxyguanosine (8-OHdG), detected via a specific antibody [45]. To quantify the expression of this marker, we set a threshold of 60 arbitrary units (a.u.) of intensity to distinguish between low and high-expressing MNs. Strikingly, KMP-treated *C9-500* animals displayed a significant reduction in high-expressing MNs compared to saline-treated animals (*C9-500* saline: 88% vs. *C9-500*+KMP: 21%) (Fig. 4A). Since the primary function of mitochondria is energy production in the form of an elevated ATP/ADP ratio, we focused on assessing whether deficits in electron transport chain (ETC) function was observed in *C9-500* spinal MNs. To this end, we used a colorimetric assay to assess Complex I, and IV activity in wildtype (*WT*) and *C9-500* spinal cord after KMP treatment. Complex I activity was measured via the NADH dehydrogenase catalyzed redox reaction in which NADH was oxidized and nitroblue tetrazolium (NBT) was reduced. The blue/purple color so formed due to NBT reduction faithfully correlates with the amount of endogenous NADH dehydrogenase activity present within cells. This blue/purple color was specifically and prominently reduced within the soma of P240 *C9-500* MNs as compared to *WT* MNs. Notably, KMP treatment

of *C9-500* mice normalized Complex I levels to *WT* levels (Fig. 4B). Subsequently, we analyzed the activity of Complex IV by determining the intensity of cytochrome c oxidation, which is detected by the brown coloring produced by the oxidation of diaminobenzidine (DAB). Like Complex I, also reduced Complex IV activity was observed within mutant *C9-500* MNs, and KMP treatment restored this deficit to normal *WT* levels (Fig. 4C). While treatment with Sal reduced UPR signaling, therefore we also explored whether Sal harbors the potential to ameliorate or restore normal mitochondrial function. Treatment with Sal did not affect the observed deficits in mitochondrial ETC levels and both Complex I (Fig. 4D) and Complex IV levels remained reduced in Sal-treated mutant MNs (Fig. 4E). Taken together these results suggest that KMP acts on both cellular organelles, reducing ER stress and promoting mitochondrial function, while Sal works selectively on inhibiting the ER stress/UPR pathway.

A short treatment regime with kaempferol selectively ameliorates behavioral hallmarks in symptomatic *C9-500* mice

Based on the observed neuroprotective action of KMP in the CNS, we assessed whether KMP treatment could rescue the behavioral defects observed in *C9-500* mouse model of *C9ORF72*-ALS. A short treatment with KMP at 10 mg/kg was performed for two weeks via daily intraperitoneal (i.p.) injections [46] as from P138-P153, an age corresponding to the appearance of the pathology-associated behavioral phenotype in *C9-500* mice [7, 29]. The reverse rotarod and hanging wire tests were performed pre-KMP treatment to obtain baseline measurement, followed by four consecutive

(See figure on next page.)

Fig. 4 Kaempferol treatment ameliorates mitochondrial function in mutant *C9-500* MNs. **a** Representative confocal images showing 8-OHdG expression levels within MNs. Quantification analyses of intensity and relative percentage of MNs expressing high and low levels of oxidative stress (low expressing MNs: *WT* saline 93%, *WT*+KMP 91%, *C9-500* saline 12%, *C9-500*+KMP 88%; high expressing MNs: *WT* saline 7%, *WT*+KMP 9%, *C9-500*+saline 88%, *C9-500*+KMP 21%. Chi square test: *WT* saline vs *C9-500*+saline; $P < 0.0001^{***}$; *C9-500*+saline vs *C9-500*+KMP: $P < 0.0001^{***}$) Scale bars: 50 μ m. **b** Representative images showing Complex I activity via the NADH dehydrogenase catalyzed redox reaction within MNs, traced with dotted red lines. Quantification analyses of staining intensity for Complex I of the mitochondria respiratory chain show that KMP treatment significantly improves Complex I activity within *C9-500* MNs. Note the negligible blue coloration for Complex I within motor neurons (Unpaired t-test, Complex I: *C9-500*+saline $n = 45$ vs *C9-500*+KMP $n = 21$, $t = 16.32$, $P < 0.0001$. Scale bars: 30 μ m. **c** Representative images showing Complex IV activity via cytochrome c oxidation, traced with dotted black lines. Quantification analyses of staining intensity for the Complex IV of the mitochondria respiratory chain reveal that KMP treatment significantly improves Complex IV activity within *C9-500* MNs. Note the pale-yellow coloration for Complex IV within motor neurons, indicative of a dysfunction in the mitochondrial respiratory chain. (Unpaired t-test, Complex IV: *C9-500*+saline $n = 21$ vs *C9-500*+KMP $n = 29$, $t = 8.449$, $P < 0.0001$). Scale bars: 30 μ m. **d** Representative images of mitochondrial respiratory Complex I staining within *C9-500* spinalMNs, traced with red dotted lines. Note the non-significant changes in Complex I levels in the spinal cord of *C9-500* treated with ER stress inhibitor Sal (Complex I, One-way ANOVA: $F = 28.35$, $P < 0.0001$, Sidak's multiple comparison test: *WT* vs *WT*+Sal, n.s.; *C9-500* vs *C9-500*+Sal, n.s. Scale bars: 100 μ m. **e** Representative images of mitochondrial respiratory Complex IV staining within *C9-500* spinal MNs, traced with black dotted lines. No changes in Complex IV levels in the spinal cord of *C9-500* treated with Sal are observed. (Complex IV One-way ANOVA: $F = 25.72$, $P < 0.0001$, Sidak's multiple comparison test: *WT* vs *WT*+Sal, n.s.; *C9-500* vs *C9-500*+Sal, n.s.). Scale bars: 100 μ m

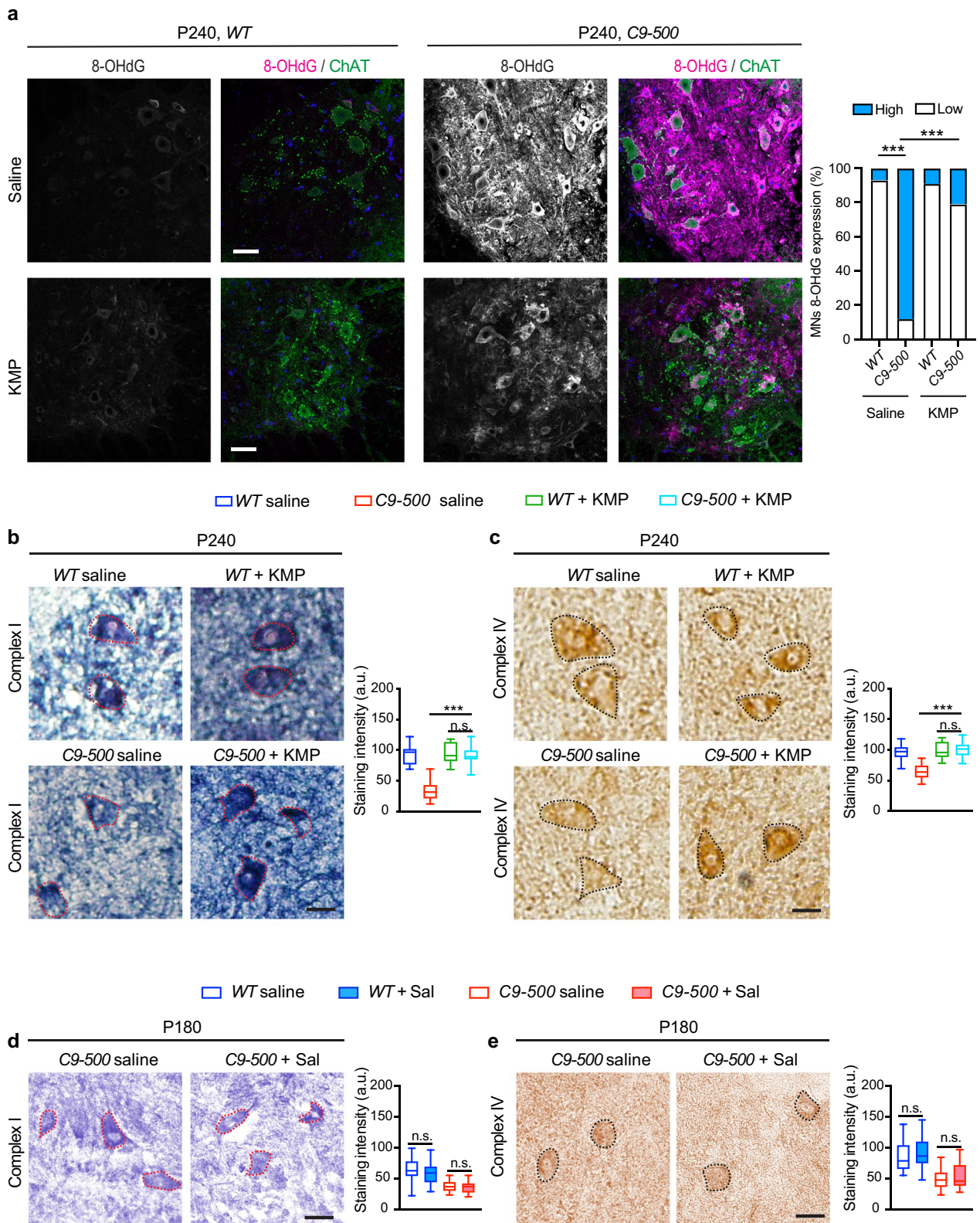


Fig. 4 (See legend on previous page.)

measurements per week post-KMP treatment for half of the cohort of mice, whereas the other half received saline (scheme Fig. 5A). Reverse rotarod assay on the *C9-500* mice cohort pre-KMP treatment revealed a striking deficit in motor performance compared to *WT* mice as observed by the dramatic decline in latency to fall measured in seconds. Notably after one week of KMP treatment *C9-500* mice presented markedly improved motor coordination and balance (Supplementary video 1 and Fig. 5B, left graph). We further continued to chronically treat the mice every alternate day with KMP until the late stage of the disease; P190, which revealed that the ameliorated rotarod performance was sustained (Fig. 5B, right graph). Similarly, the hanging wire test revealed that after two weeks of KMP treatment, the average number of falls within the two minutes was reduced compared to the performance of the same cohort of mice pre-KMP treatment (Fig. 5C). Likewise, the time taken to first fall improved slightly between pre- and post-KMP treatment, suggesting that KMP treatment led to an overall amelioration in muscle endurance and function (Fig. 5D). We next assessed whether another compound; Sal which is known to inhibit ER stress and has been shown to ameliorate ALS-associated pathological symptoms in other

familial ALS mouse models [5, 47, 48], could also have a beneficial outcome in *C9-500* mice. Like KMP treatment regime, Sal treatment was performed on symptomatic P145 *C9-500* mice lasting until P170 (Fig. 5E). This treatment led to no improvement in the reverse rotarod performance (Fig. 5F). Moreover, hanging wire tests revealed no significant amelioration in muscle endurance or stamina as measured by number of falls within two minutes (Fig. 5G) or time to the first fall (Fig. 5H). It is noteworthy that unlike studies done on *SOD1-G93A* mice, wherein Sal treatment was neuroprotective [5], in the *C9-500* mice model, we found no protective effect of Sal, indicative of a likely more complex interplay between various cellular impairments ranging from mitochondrial dysfunction to proteostasis and autophagy thus, leading to an accumulation of toxic events resulting in the development of the symptomatic pathology.

Kaempferol potentially elicits its action by binding to GRP75

We sought to understand how KMP could dually act on inhibiting ER stress while sustaining mitochondrial function. We hypothesized that KMP likely exerts its effect at mitochondrial-associated membranes (MAM),

(See figure on next page.)

Fig. 5 Kaempferol but not Salubrinal trt. rescues behavioral phenotype in symptomatic *C9-500* mice. **a** Schematic depiction of the experimental timeline for in vivo treatment of symptomatic *C9-500* mice with KMP. Initial short treatment lasting for two weeks was performed by daily intraperitoneal (i.p.) injection of KMP. This was followed by injection every alternate day up to P190. **b** Reverse rotarod plotted as latency to fall, *C9-500* mice treated with KMP show significant improvement in motor performance compared to *C9-500* saline treated group. Note the substantial improvement in motor performance to near normal *WT* levels, already one week after KMP treatment, which is sustained after two weeks of KMP treatment as well as until late disease stage at P190. (Number of animals: 10 *WT*+saline; 10 *C9-500*+saline; 10 *WT*+KMP; and 11 *C9-500*+KMP). Two-way ANOVA: interaction $P < 0.0001^{***}$, $F(15,216) = 21.95$, time $P < 0.0001^{***}$ $F(5,216) = 197.2$, treatment $P < 0.0001^{***}$, $F(3,216) = 580.1$, Bonferroni post hoc. *WT*+saline vs *C9-500*+saline *** ; *C9-500*+saline vs *C9-500*+KMP *** . **c** Hanging wire test showing muscle performance in *WT* and *C9-500* mice before and after KMP treatment. The total number of falls within a period of 2 min were significantly higher in *C9-500* mice group than *WT* mice cohort. However, continuous KMP treatment significantly reduced the number of falls within *C9-500* after KMP treated group as compared to *C9-500* before KMP treatment (Number of animals: 10 *WT* pre-trt., 10 *C9-500* pre-trt.; 10 *WT*+KMP; and 10 *C9-500*+KMP). One way ANOVA: $P < 0.0001^{***}$ $F = 18.15$, Sidak's multiple comparisons: *WT* pre-trt. vs *C9-500* pre-trt. *** ; *C9-500* pre-trt. vs *C9-500*+KMP (2 weeks) *** . **d** Hanging wire test showing muscle performance in *WT* and *C9-500* mice before and after KMP treatment. No significant difference was observed in the *C9-500* mice cohort in the timing to first fall after one week of KMP treatment, but significant improvement was observed after 2 weeks of KMP treatment. number of falls, One way ANOVA: $P < 0.0001^{***}$ $F = 13.84$, Sidak's multiple comparisons: *WT* pre-trt. vs *C9-500* pre-trt. *** ; *C9-500* pre-trt. vs *C9-500*+KMP (2 weeks) n.s. Time to first fall; One way ANOVA: $P < 0.0001^{***}$, $F = 9.246$, Sidak's multiple comparisons: *WT* pre-trt. vs *C9-500* pre-trt. ** ; *C9-500* pre-trt. vs *C9-500*+KMP n.s. **e** Schematic depiction of the experimental timeline for in vivo treatment of symptomatic *C9-500* mice with Sal, which was performed by intraperitoneal (i.p.) injection of Sal every alternate day to avoid nephrotoxicity in mice. Treatment was stopped at P170, following the animal ethics guidelines as no beneficial effect of the treatment was observed. **f** Inverse Rotarod test presented as latency to fall, does not show significant improvement in *C9-500* mice after Sal treatment (Two-way ANOVA: interaction $F(9,92) = 0.9044$, n.s.; Age $F(3,92) = 5.3^{**}$; treatment $F(3,92) = 120^{***}$, Sidak's multiple comparisons test *C9-500*+saline vs *C9-500*+Sal: P140 n.s.; P150 n.s.; P160 n.s.; P170 n.s.). $n = 6$ *WT*+saline, 6 *WT*+Sal, $n = 8$ *C9-500*+saline, $n = 8$ *C9-500*+Sal. **g** Hanging wire test performed at P140 and P170, showing no significant improvement in *C9-500* animals after Sal treatment in the average number of falls within a period of 2 min. (One way ANOVA no. of falls: $F = 34.60^{***}$, Sidak's multiple comparison at P140: *WT*+saline vs *C9-500*+saline *** , *WT*+Sal vs *C9-500*+Sal *** , *C9-500*+saline vs *C9-500*+Sal n.s.; at P170: *WT*+saline vs *C9-500*+saline *** , *WT*+Sal vs *C9-500*+Sal *** , *C9-500*+saline vs *C9-500*+Sal n.s.). **h** Hanging wire test performed at P140 and P170, showing no significant improvement in the time taken to first fall is observed in *C9-500* animals after Sal treatment (One way ANOVA average time to first fall: $F = 31.96^{***}$, Sidak's multiple comparisons at P140: *WT*+saline vs *C9-500*+saline *** , *WT*+Sal vs *C9-500*+Sal *** , *C9-500*+Saline vs *C9-500*+Sal n.s.; at P170: *WT*+saline vs *C9-500*+saline *** , *WT*+Sal vs *C9-500*+Sal *** , *C9-500*+saline vs *C9-500*+Sal n.s.)

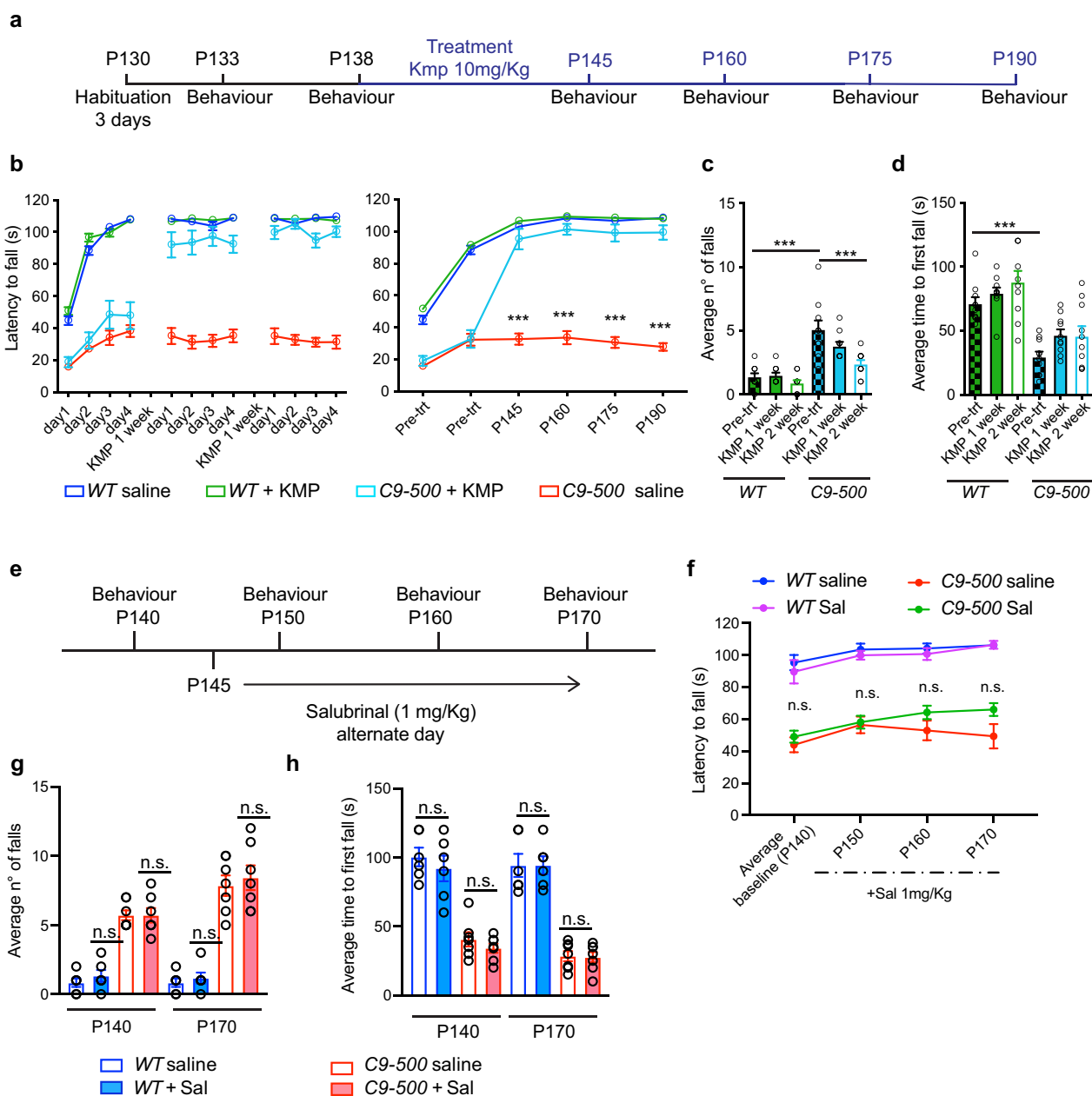


Fig. 5 (See legend on previous page.)

representing regions of contact between the ER and mitochondria. MAM constitutes regions of ER membranes that are reversibly tethered to mitochondria. These membranes are involved in the import of specific lipids from the ER to mitochondria and the regulation of Ca^{2+} homeostasis, mitochondrial function, autophagy, and apoptosis [49, 50]. We performed an in-silico search for potential KMP interactors, which likely function at the MAM. The structure of KMP was uploaded to CB-Dock (<http://clab.labshare.cn/cb-dock/php/dockingresult.php>)

for analysis of the docking potential of KMP to MAM-located molecules. These analyses led to the identification of GRP75 (75-kDA glucose-regulated protein) as being the strongest binding partner of KMP as indicated by the vina score. GRP75 is a major mitochondrion located chaperone, which interacts with the component of both the mitochondrial quality control system and MAMs, thus playing a key role in mitochondrial homeostasis (Fig. 6A). The crystal structure of GRP75 revealed a significant interaction of KMP with the nucleotide-binding

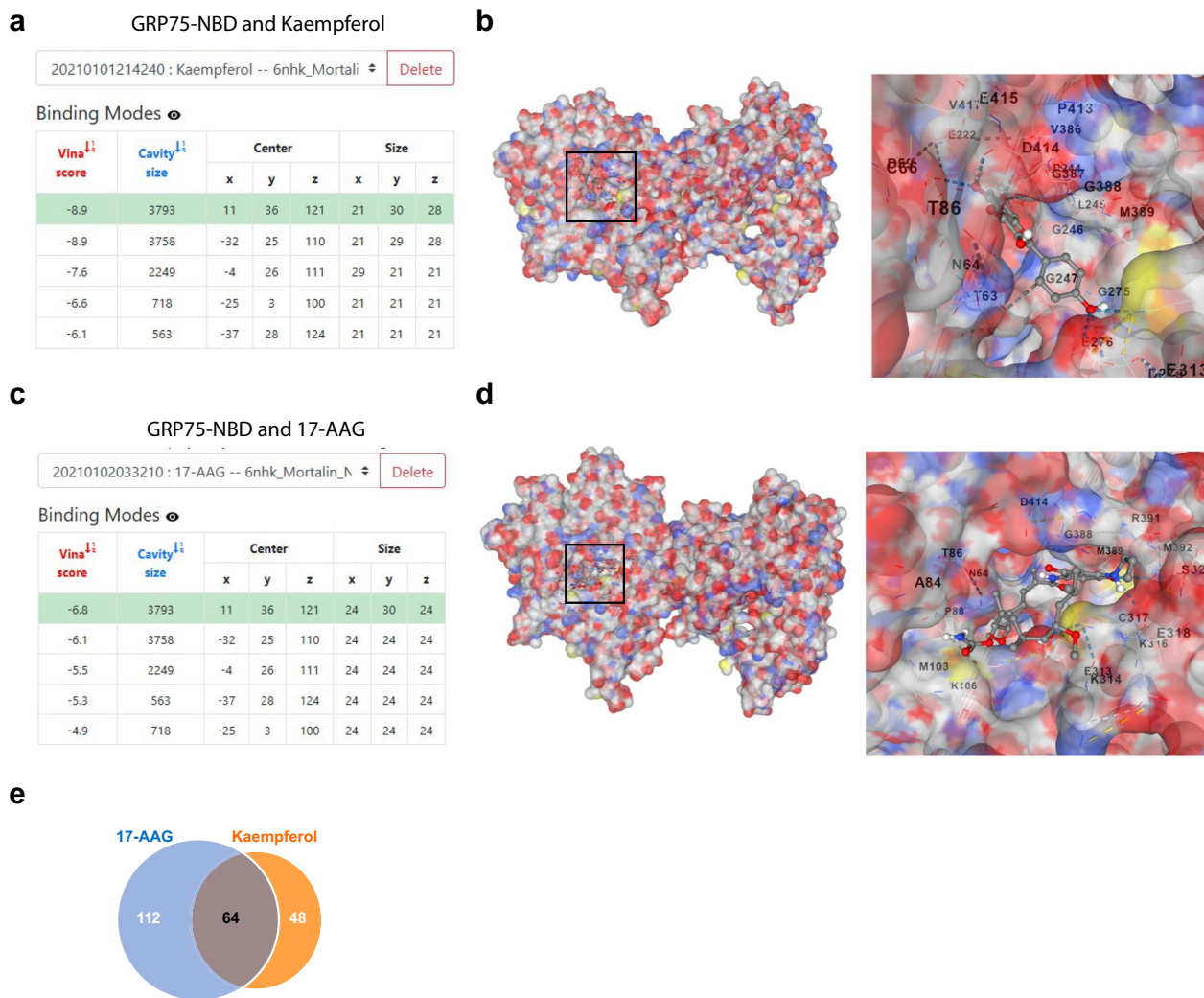


Fig. 6 In silico modeling reveals preferential Kaempferol binding to the nucleotide-binding domain of GRP75. **a** Table depicting Vina scores, and cavity information of the docking simulation pose for GRP75 nucleotide-binding domain (NBD) and KMP. **b** The structure of KMP was uploaded to CB-Dock for analysis of the docking potential with GRP75. The crystal structure of the human GRP75 nucleotide-binding domain (PDB ID: 6NHK), the active site is colored white (carbon), red (oxygen), blue (nitrogen), and yellow (sulphur). The crystal pose of the ligand KMP in the cavity sized 3793 is colored white (hydrogen), grey (carbon), and red (oxygen). **c** Table depicting Vina scores, and cavity information of the docking simulation pose for GRP75 nucleotide-binding domain (NBD) and 17-AAG. **d** The crystal structure of the human GRP75 nucleotide-binding domain (PDB ID: 6NHK), the active site is colored white (carbon), red (oxygen), blue (nitrogen), and yellow (sulphur). The crystal pose of the ligand 17-AAG in the cavity sized 3793 is colored white (hydrogen), grey (carbon), and red (oxygen). Note the comparatively lower Vina score for 17-AAG binding to GRP75-NBD compared to that of KMP within the same pocket, suggesting a stronger fit of KMP in the NBD domain of GRP75. **e** Venn diagram depicting the number of overlapping human proteins that are targeted by both KMP and 17-AAG. The PharmMapper database was used to predict the targets of Kmp and 17-AAG. This mapping predicted a large overlap of targets shared (cut-off z-score: 0.5) by the two compounds, including HSP90A. Both ligands did not target GRP75. See Suppl. Table 1 for the complete list of overlapping targets

domain (NBD) of GRP75 (Fig. 6B). We further assessed if other molecules could show similar interaction with GRP75 and found that 17-AAG had the second highest Vina score for binding to GRP75 (Fig. 6C) and strongly docked to the NBD site of GRP75 (Fig. 6D). Further, analyses revealed that a substantial number of overlapping human proteins were targeted by both KMP and 17-AAG (Fig. 6E and Suppl. Table 1). However, literature

analysis revealed that 17-AAG indirectly increases the expression level of GRP75 [51], while inhibiting HSP90 chaperone family, thereby impairing protein folding of multiple client substrates and autophagy that is impaired in *C9ORF72*-ALS. KMP enhances mitochondrial Ca²⁺ uptake, by a yet unidentified mechanism involving the binding to the mitochondrial uniporter, in traumatic brain injury model (TBI) [52]. Interestingly, no binding

affinity of Sal to GRP75 was observed (data not shown). Since a previous study from us has shown reduced GRP75 expression at the MAM in *C9-500* mice and its pathological sequestration by Poly(GA) aggregates within neurons, therefore we focussed on assessing whether KMP could exert neuroprotection via modulating GRP75 expression or mode of action, thus counteracting both ER and mitochondrial deficits.

Kaempferol enhances IP3R-VDAC1 interactions, promoting optimal mitochondrial function via GRP75

Based on our in-silico screening, we hypothesized that the mechanism behind KMP-mediated neuroprotection could be via its interaction with GRP75 at the MAM. Since GRP75 serves as a scaffold, bringing iP3R-VDAC1 in proximity, we firstly, assessed iP3R-VDAC1 interactions via proximity ligation assay (PLA). Chronic, KMP treatment from symptomatic stage until the end stage of disease revealed increased iP3R-VDAC1 interactions versus saline-treated mutant spinal MNs of *C9-500* mice (Fig. 7A). Since saline-treated mutant *C9-500* MNs revealed dramatically reduced iP3R-VDAC1 interactions compared to *WT* MNs, and this reduced interaction was normalized after KMP treatment, indicated that KMP could potentially attenuate mitochondrial dysfunction by promoting optimal Ca^{2+} uptake by mitochondria. Thus, we examined the physiological process of Ca^{2+} uptake by mitochondria, which majorly occurs at the ER–mitochondria contact sites via iP3R-VDAC1. To this end, cortical neurons from *WT* and *C9-500* neonates were cultured and we measured mitochondrial Ca^{2+} uptake. Fluo-4AM was combined with an intracellular buffer that eliminated cytosolic and ER Ca^{2+}

signals [34], thereby enabling specifically the measurement of mitochondrial Ca^{2+} uptake. A striking deficit was observed in mitochondrial Ca^{2+} uptake in *C9-500* cortical neurons as observed by significantly reduced Ca^{2+} transients compared *WT* cortical neurons. These deficits in Ca^{2+} uptake by mutant mitochondria were efficiently eliminated by treating cortical neurons with KMP, confirming our finding that KMP elicits its effect at the MAM, modulating the mitochondrial uptake of Ca^{2+} (Fig. 7B). We next measured GRP75 expression in spinal MNs to assess whether KMP modulates GRP75 expression. MNs from both *WT* and *C9-500* mice treated with KMP displayed augmented GRP75 expression (Fig. 7C). Of note the degree of enhanced GRP75 expression was much higher in mutant *C9-500* MNs, as they present dramatically reduced GRP75 expression at late stages of the disease. To underpin the molecular mechanism associated with the beneficial effect of GRP75 on the mitochondria, we co-immunoprecipitated GRP75 from P125, *C9-500* and *WT* ventral spinal cord, followed by mass spectrometric (MS) analyses. The interactome of GRP75 revealed known interactions such as those with VDAC1 as well as other interactions shared between the two genotypes (Suppl. Table 2). We focused on GRP75 interactions, which were strongly present in the *C9-500* spinal cord. Within the top five GRP75 interacting proteins, as measured semi-quantitatively via peptide match score summation (PMSS), was mitochondrial ATP synthase-coupling factor 6 (ATP5J), (Fig. 7D). ATP5J produces ATP from ADP in the presence of a proton gradient across the mitochondrial membrane, generated by the ETC of the respiratory chain, we validated the interaction between ATP5J and GRP75 in *C9-500* MNs using

(See figure on next page.)

Fig. 7 Kaempferol enhances IP3R and VDAC1 association promoting mitochondrial Ca^{2+} uptake. **a** Representative images of proximity ligation assay (PLA) between IP3R and VDAC1 in *C9-500*+saline and *C9-500*+KMP treated mice, showing a notable increase in the number of puncta in *C9-500*+KMP treated animals (One-way ANOVA: $F = 100.0$, $P < 0.0001^{***}$, Sidak's multiple comparison test: *WT*+saline vs *C9-500*+saline, $t = 5.303$, *** ; *C9-500*+saline vs *C9-500*+KMP, $t = 16.31$, ***). Scale bar = 10 μm , $n = 3\text{--}4$ mice per genotype/treatment. **b** Baseline and stimulated mitochondrial Ca^{2+} uptake traces in *WT* and *C9-500* cortical neurons (dotted lines) and after KMP treatment (bold lines). KMP treatment significantly improves Ca^{2+} uptake in the mitochondria of *C9-500* cortical neurons (number of neurons *WT*: 22, *C9-500*: 24, *WT*+KMP:21, *C9-500*+KMP: 21; multiple t-test 100 s *C9-500* mean = 0.967, *C9-500*+KMP mean = 2.285, $P < 0.0001$). **c** Representative confocal images of spinal cord immunolabeled for GRP75 shows a significant increase in *C9-500* and *WT* MNs treated with KMP (One-way ANOVA $F = 102.8$, $P < 0.0001^{***}$, Sidak's multiple comparison test: *WT* saline vs *C9-500* saline $t = 6.203$, *** ; *C9-500* saline vs *C9-500*+KMP $t = 16.42$, ***). Scale bars: 30 μm . **d** List of proteins found to specifically interact with GRP75 in *C9-500* ventral spinal cord but not in *WT* after mass spectroscopy (MS) analysis of immunoprecipitation for GRP75. Specifically, in red are highlighted GRP75 and VDAC1 as an internal control of the experiment (present in both *WT* and *C9-500* samples), and in green is highlighted ATP5J (ATP synthase factor 6 of the mitochondria), whose interaction with GRP75 was detected in *C9-500* ventral spinal cord lysates, which are enriched for MNs. **e** PLA between ATP5J and GRP75 in *WT* and *C9-500* at P125 and P200, showing notable increase in number of puncta in *C9-500* at P125 when MNs express high levels of GRP75 (Unpaired t-test P125 *WT* vs *C9-500*, $t = 25.28$, *** ; P200 *WT* vs *C9-500*, $t = 3.58$, ***). **f** Representative confocal images of *WT* and *C9-500* MNs stained for GRP75 and ATP5J. MNs expressing high levels of GRP75 also express high levels of ATP5J. Right: Q.A of ATP5J expression across different disease stages: One-way ANOVA $F = 95.75$, $P < 0.0001^{***}$; Sidak's multiple comparison test: P30 *WT* $n = 26$ vs P30 *C9-500* $n = 46$, $t = 0.4823$, n.s.; P125 *WT* $n = 42$ vs P125 *C9-500* $n = 59$, $t = 16.29^{***}$, P200 *WT* $n = 27$ vs P200 *C9-500* $n = 27$, $t = 3.795^{***}$. Scale bars: 30 μm . **g** Representative images of ATP5J staining depicting the increased intensity of ATP5J expression in *WT* and *C9-500* treated with KMP (One-way ANOVA: $F = 90.48$, $P < 0.0001^{***}$, Sidak's multiple comparison test: *WT* saline vs *WT*+KMP $t = 4.928$, *** ; *C9-500* saline vs *C9-500*+KMP $t = 15.55$, ***). Scale bars: 10 μm

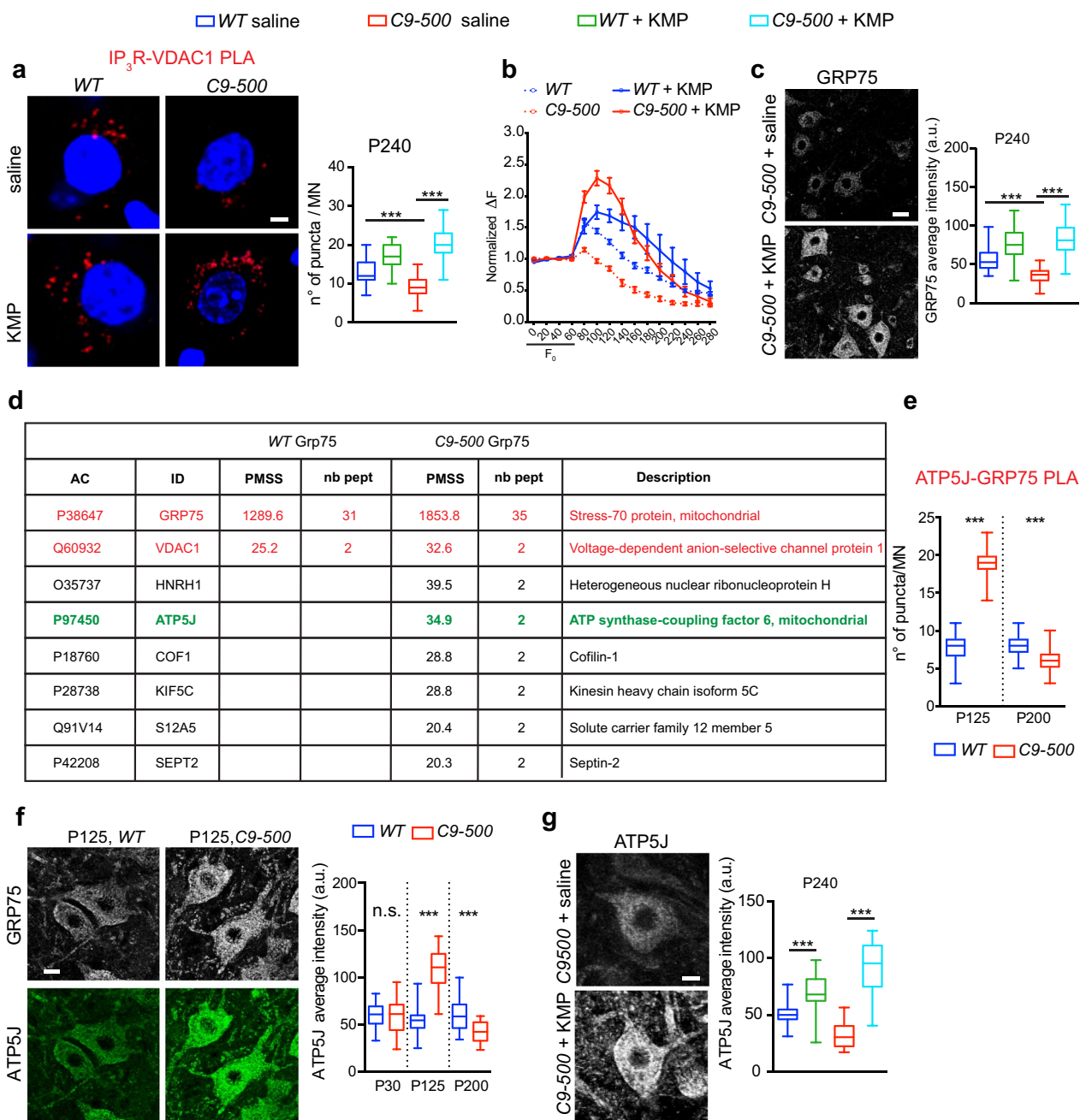


Fig. 7 (See legend on previous page.)

PLA. Endogenous GRP75 interactions with ATP5J was observed in both *WT* and *C9-500* MNs, albeit strongly at P125 mutant MNs. However, akin to reduced *iP3R-VDAC1* interactions at P240, *ATP5J-GRP75* were much lower in late-stage mutant MNs, indicative of advanced mitochondrial dysfunction and degeneration (Fig. 7E). As KMP treatment augmented GRP75 expression, we examined *ATP5J* expression in response to KMP treatment. While *ATP5J* levels were reduced in P240 MNs,

likely reflecting the reduced GRP75 expression, spinal MNs treated with KMP even at end stage presented high *ATP5J* immunoreactivity, reflecting an overall beneficial effect of KMP on mitochondria via the GRP75-*ATP5J* pathway (Fig. 7F).

Discussion

ALS is a multifactorial disease, with complex overlapping clinical symptoms, and a fatal outcome within 3–5 years of diagnosis [53, 54]. Several studies have indicated that ER stress plays a pivotal role in the pathophysiology of ALS [2, 55], thus targeting ER stress is an interesting objective for therapeutic intervention. Besides, ER stress, mitochondrial dysfunction associated with oxidative stress, mitochondrial Ca^{2+} uptake deficits and bioenergetic deficits is closely associated with ALS pathophysiology [56–59], therefore identifying compounds that can alleviate both mitochondrial and ER impairments in ALS is extremely important to the field of ALS. In this study, we identified and explored the potential of a dietary flavanol KMP as a modulator of both ER stress response as well as mitochondria function in ALS. Focussing on the most common genetic form of ALS, *C9ORF72*-linked ALS, we show that KMP harbours the potential to attenuate ER stress and UPR signaling in vivo in symptomatic *C9-500* rodent MNs as well as in vitro in human *C9ORF72* patient-derived iMNs. Moreover, we provide compelling evidence for the ability of KMP to restore ATP production and normalize mitochondrial function in *C9ORF72* ALS. This is noteworthy, as previous compounds such as Sal have been shown to interfere only with the PERK/ P_i -eIF2 α -UPR pathway [5, 10, 60], or by suppressing the activity of integrated stress response, upstream of the PERK/ P_i -eIF2 α -UPR pathway [37]. Moreover, drugs like Sal or guanabenz enhance the persistent translation inhibition by P_i -eIF2 α , thereby, accelerating neurodegeneration in a model of prion disease [61] or in mutant male SOD1 mice [62]. In addition, both these compounds elicit toxicity on other organelles such as nephrotoxicity observed after chronic Sal administration [63] or blood pressure dysregulation after guanabenz administration [64]. These studies highlight the unmet need for a drug candidate with the ability to reduce UPR signaling in affected neurons, without side effects. In this context, KMP and its derivatives are natural dietary phytochemicals, lacking evident toxicity, and are known to exhibit antioxidant, anti-inflammatory, anticancer, and neuroprotective activity [65].

Notably, we found that treatment with KMP initiated after the onset of pathological symptoms was able to abrogate intrinsic mitochondrial deficits present in *C9ORF72* neurons. These data are remarkable, as KMP normalized mitochondrial ATP levels in human *C9ORF72* iMNs, an important determinant of overall adequate neuronal energy supply and optimal function. While Sal as expected, did inhibit ER stress, it did not ameliorate mitochondrial function either in vivo in *C9-500* MNs or in vitro in human iMNs. On the contrary, Sal has been shown to promote cell death in cancer by

activating the ISR and inducing mitochondrial oxidative stress, thereby irreversibly damaging mitochondria. Further, Sal treatment in glucose-deprived conditions leads to the upregulation of mitochondrial ROS, thereby inducing mitochondrial stress and dysfunction [66]. Our finding that KMP ameliorated mitochondrial dysfunction and inhibited ER stress may be linked to its ability to regulate Ca^{2+} signaling, especially as a key process that links these ER-mitochondria interactions. The transfer of Ca^{2+} from the ER to mitochondria via the MAMs may lead to either pro-survival or pro-death effects, likely contributing to elevated mitochondrial ATP generation to cope with increased energy demands during mitochondrial stress. Conversely, enhanced mitochondrial Ca^{2+} may promote apoptosis [67]. Previous studies have shown that KMP alleviates oxidative stress and apoptosis during lung ischemia–reperfusion injury, by enhancing mitochondrial membrane potential and inhibiting the opening of mitochondrial permeability transition pores [68]. Importantly, KMP has been shown to control mitochondrial Ca^{2+} regulation by directly activating the mitochondrial Ca^{2+} uniporter (MCU) in a concentration-dependent manner. Even at a low concentration such as 1 μM of KMP treatment, practically doubled the uptake of mitochondrial Ca^{2+} [69]. Moreover, recent studies, have also identified a mitochondria-mediated control of the UPR signaling. PIGBOS; a microprotein localized to the mitochondrial outer membrane controls UPR responses during stress. PIGBOS interacts with the ER protein CLCC1 at MAM contact sites and changes in PIGBOS expression led to enhanced UPR and increased cell death [70]. Therefore, based on our findings, it is very likely that KMP treatment harbors the ability to counteract mitochondrial Ca^{2+} uptake deficits and dysfunction in *C9ORF72*-ALS [6, 7], thus reducing mitochondrial stress and promoting optimal mitochondrial function and neuroprotection. KMP has been shown to modulate key signaling pathways involved in neurodegeneration and neuroinflammation, such as the PI3K/Akt, MAPK/ERK, and NF- κ B pathways, nevertheless, further research is necessary to decipher the underlying mechanisms of action, to optimize dosage schedules, and assess the safety and efficacy of this intervention in human clinical trials.

Of note, administration of KMP via the i.p. route at symptomatic ages in *C9-500* mice attenuated the accumulation of large Poly(GA) aggregates, increased the number of surviving MNs, and improved motor behaviour. We believe that these findings enhance the predictive value that KMP could be beneficial in patients with *C9ORF72*-ALS and in other familial forms of ALS, where ER stress and mitochondrial impairments occur together with mutant protein inclusions. In other

neurodegenerative diseases such as Alzheimer's disease, KMP treatment inhibited β -A structure formation by hindering amyloid fibril elongation [71]. Yet in another study treatment with KMP derivative; kaempferide revealed the enhanced expression of the brain-derived neurotrophic factor (BDNF), which in turn augmented the phosphorylation of transcription factor cAMP, thus promoting synaptic plasticity [72]. In Parkinson's disease, KMP ameliorated nigrostriatal dopaminergic neuron lesions; by inhibiting interleukin (IL) 1 β , IL-6, and TNF α production, highlighting the anti-inflammatory activity of KMP [73].

The mechanism via which KMP elicits its anti-ER stress properties remains unclear. However, studies have shown that KMP inhibits the expression of BiP, thereby inhibiting the activation of UPR sensors PERK, ATF6, and IRE1 [17]. These findings fit well with our observations of reduced BiP and P_i-eIF2 α expression after KMP treatment. Our data from in silico modeling identified that KMP strongly binds to GRP75; a chaperone located within the mitochondria, but is majorly involved at the MAM, functioning as a structural scaffold protein for the iP3R-VDAC1 channel. This channel is the most prominent channel at the MAM promoting optimal transfer of Ca²⁺ from the ER to the mitochondria. GRP75 expression levels are progressively reduced in *C9-500* mice, and those reductions coincide with the onset of UPR signaling and the appearance of large Poly(GA) inclusions within MNs [7]. Our PLA data suggests that within the *C9-500* spinal MNs, KMP enhances iP3R-VDAC1 interactions, which aids in the optimal mitochondrial Ca²⁺ uptake, important for the proper ETC process. Of note, our data also revealed the ability of KMP to enhance the expression of GRP75 and its interacting partner ATP5J in MNs, suggesting that KMP could act on the process regulating protein translation. Interestingly, like quercetin yet another flavanol, KMP might positively modulate gene expression [27, 28]. However, further experiments are needed to dissect how KMP impacts GRP75 expression and iP3R-VDAC1 function in the context of *C9ORF72*-ALS.

Given the translation potential of our findings, we measured ER stress and mitochondrial function in human *C9ORF72* patient-derived iMNs and found that KMP not only ameliorated ER stress and restored normal mitochondrial function in three different *C9ORF72*-patient iMN lines, but also provided neuroprotection by promoting iMNs survival in the presence of ER stress. To the best of our knowledge, no previous drug compound has been reported to have a protective effect in *C9-500* mice by dually ameliorating ER stress and mitochondrial function. Concomitantly, the reduction in large Poly(GA) aggregates, sustained motor neuron survival,

and improved muscle and behavioral phenotype highlight the beneficial potential of KMP in the *C9-500* mice, when treatment was initiated at disease signs onset. This is a clinically relevant time point for the initiation of therapy in human patients, as usually, they do not receive a diagnosis before symptoms onset. Additionally, we identified a novel mode of action of KMP, via the regulation of GRP75 expression and function. These observations suggest that KMP is a likely strong candidate for the prevention/slowing down of disease pathology in familial ALS cases and could support future combinatorial therapies such as the dual treatment with the approved medication Riluzole that reduces excitotoxicity in ALS.

In conclusion, KMP rescues motor neuron survival in vitro and in vivo by regulating the ER stress response and ameliorating intrinsic mitochondrial function, which are key pathways implicated in the pathophysiology of *C9ORF72*-ALS. Although the precise mode of action of KMP remains incomplete, our data suggests that one likely pathway involves the interaction with the nucleotide-binding domain of GRP75, thus enhancing/stimulating GRP75 activity. Hence, KMP is a promising compound for diseased MNs, meriting further study as a promising drug candidate in ALS.

Abbreviations

ALS	Amyotrophic lateral sclerosis
a.u.	Arbitrary units
Ca ²⁺	Calcium
dNs	Direct reprogramming of fibroblasts to neurons
FTD	Frontal temporal dementia
iPSC	Induced pluripotent stem cells
ISR	Integrated stress response
iMNs	iPSC-derived motor neurons
KMP	Kaempferol
Min	Minutes
MAMs	Mitochondria-associated membranes
MNs	Motor neurons
PTPIP51	Protein tyrosine phosphatase interacting protein 51
Sal	Salubrinal
TU	Tunicamycin
UPR	Unfolded Protein response

Supplementary Information

The online version contains supplementary material available at <https://doi.org/10.1186/s40478-025-01927-y>.

Supplementary material 1: Figure S1. Representative images: 2-week-old iMNs derived from Control (1) immunolabeled for the neuronal marker MAP2 and the motor neuron marker Chat. Scale bars: 30 μ m, zoom: 15 μ m.

Supplementary material 2: Table S1. List of overlapping human proteins targeted by both kaempferol and 17-AAG. Supplementary Table 2: The interactome of GRP75 as revealed by mass spectrometry analyses, note the strong interaction between the established association of GRP75 with VDAC1.

Supplementary material 3: Video: Inverse rotarod measurement showing ameliorated motor coordination in *C9-500* mice after Kaempferol treatment

Acknowledgements

We thank Pentti Tienari, Helsinki University Central Hospital, Finland, Biomedicum Stem Cell Center, GoEditStem platform, HiLIFE, Helsinki, Finland; Bhuvanesh T. Selvaraj and Siddharthan Chandran, UK Dementia Research Institute, University of Edinburgh, UK, Euan MacDonald Centre for MND Research, University of Edinburgh, UK for providing iPSC cell lines. We thank Manfred Heller, Proteomic Core Facility, Department for BioMedical Research, University of Bern for Mass spectrometry. We also thank Nicolas Charlet-Berguerand, Institut de Génétique et de Biologie Moléculaire et Cellulaire (INSERM U964, CNRS UMR7104 for Poly(GA) antibody, Angelina Oestmann and Maria Essers for maintaining mouse colonies and helping with behavioral assays and all Saxena lab members for support and discussions.

Author contributions

F.P., S.S. conceived the study and wrote the manuscript. F.P., performed experiments and data analyses with contributions from P.H.S., R.D., and J.A.S.D. M.S. and O.J. performed muscle histology and analyses. O.S. and S.S. provided reagents. S.S. supervised the overall project, all authors read and commented on the manuscript.

Funding

This study was funded by the SPINAL CORD INJURIES/DISEASE RESEARCH PROGRAM (SCIDRP), University of Missouri, Missouri, USA, European Research Council (ERC) under the European Union's Horizon 2020 research and innovation program (grant agreement #725825), Swiss National Science Foundation, Swiss Foundation for Research on Muscle Diseases, and E-rare grant (CALSER) to S.S.

Data availability

No datasets were generated or analysed during the current study.

Declarations

Animal experiments

The study was approved by the Animal Commission of Canton of Bern, Switzerland, license number BE-35/17, BE-82/18.

Human fibroblast-derived cells

Cells were anonymized and provided to us under an MTA from respective consortia. Culturing of cells only did not require internal review board (IRB) approval.

Consent for publication

All authors have approved the manuscript and agree with its submission.

Competing interests

The authors declare that they have no competing interests.

Author details

¹Department of Physical Medicine and Rehabilitation, University of Missouri, Columbia, MO, USA. ²NextGen Precision Health, University of Missouri, Columbia, MO, USA. ³Institut Neuromyogène, Pathophysiology and Genetics of the Neuron and Muscle, Inserm U1315, CNRS, Université Claude Bernard Lyon I, UMR 5261, 69008 Lyon, France. ⁴Department of Neurology, Inselspital University Hospital, Bern, Switzerland.

Received: 2 October 2024 Accepted: 6 January 2025

Published online: 01 February 2025

References

- Halliday M, Mallucci GR (2014) Targeting the unfolded protein response in neurodegeneration: a new approach to therapy. *Neuropharmacology* 76:169–174
- Hetz C, Saxena S (2017) ER stress and the unfolded protein response in neurodegeneration. *Nat Rev Neurol* 13:477–491
- Rozpędek-Kamińska W, Siwecka N, Wawrzynkiewicz A, Wojtczak R, Pytel D, Diehl JA et al (2020) The PERK-dependent molecular mechanisms as a novel therapeutic target for neurodegenerative diseases. *Int J Mol Sci* 21:2108
- Kim S, Kim DK, Jeong S, Lee J (2022) The common cellular events in the neurodegenerative diseases and the associated role of endoplasmic reticulum stress. *Int J Mol Sci* 23:5894
- Saxena S, Cabuy E, Caroni P (2009) A role for motoneuron subtype-selective ER stress in disease manifestations of FALS mice. *Nat Neurosci* 12:627–636
- Dafinca R, Barbagallo P, Farrimond L, Candaliya A, Scaber J, Ababneh NA et al (2020) Impairment of mitochondrial calcium buffering links mutations in C9ORF72 and TARDBP in iPS-derived motor neurons from patients with ALS/FTD. *Stem Cell Rep* 14:892–908
- Pilotto F, Schmitz A, Maharjan N, Diab R, Odriozola A, Tripathi P et al (2022) PolyGA targets the ER stress-adaptive response by impairing GRP75 function at the MAM in C9ORF72-ALS/FTD. *Acta Neuropathol (Berl)* 144:939–966
- Mori K, Arzberger T, Grässer FA, Gijssels I, May S, Rentsch K et al (2013) Bidirectional transcripts of the expanded C9orf72 hexanucleotide repeat are translated into aggregating dipeptide repeat proteins. *Acta Neuropathol (Berl)* 126:881–893
- Schmitz A, Pinheiro Marques J, Oertig I, Maharjan N, Saxena S (2021) Emerging perspectives on dipeptide repeat proteins in C9ORF72 ALS/FTD. *Front Cell Neurosci* 15:637548
- Jiang J, Ravits J (2019) Pathogenic mechanisms and therapy development for C9orf72 amyotrophic lateral sclerosis/frontotemporal dementia. *Neurother J Am Soc Exp Neurother* 16:1115–1132
- Mehta AR, Gregory JM, Dando O, Carter RN, Burr K, Nanda J et al (2021) Mitochondrial bioenergetic deficits in C9orf72 amyotrophic lateral sclerosis motor neurons cause dysfunctional axonal homeostasis. *Acta Neuropathol (Berl)* 141:257–279
- Wang T, Liu H, Itoh K, Oh S, Zhao L, Murata D et al (2021) C9orf72 regulates energy homeostasis by stabilizing mitochondrial complex I assembly. *Cell Metab* 33:531–546.e9
- Barazzuol L, Giamogante F, Cali T (2021) Mitochondria Associated Membranes (MAMs): architecture and physiopathological role. *Cell Calcium* 94:102343
- Markovinovic A, Greig J, Martín-Guerrero SM, Salam S, Paillusson S (2022) Endoplasmic reticulum-mitochondria signaling in neurons and neurodegenerative diseases. *J Cell Sci* 135:jcs248534
- De Vos KJ, Mórotz GM, Stoica R, Tudor EL, Lau K-F, Ackerley S et al (2012) VAPB interacts with the mitochondrial protein PTP1P51 to regulate calcium homeostasis. *Hum Mol Genet* 21:1299–1311
- Gomez-Suaga P, Mórotz GM, Markovinovic A, Martín-Guerrero SM, Preza E, Arias N et al (2022) Disruption of ER-mitochondria tethering and signaling in C9orf72-associated amyotrophic lateral sclerosis and frontotemporal dementia. *Aging Cell* 21:e13549
- Abdullah A, Ravanan P (2018) Kaempferol mitigates endoplasmic reticulum stress induced cell death by targeting caspase 3/7. *Sci Rep* 8:2189
- Yu X, Ren Z, Wang Y, Yuan G, Hu J, Song L et al (2024) Kaempferol attenuates particle-induced osteogenic impairment by regulating ER stress via the IRE1 α -XBP1s pathway. *J Biol Chem* 300:107394
- Wang H, Chen L, Zhang X, Xu L, Xie B, Shi H et al (2019) Kaempferol protects mice from d-GalN/LPS-induced acute liver failure by regulating the ER stress-Grp78-CHOP signaling pathway. *Biomed Pharmacother Biomedicine Pharmacother* 111:468–475
- Yu L, Chen C, Wang L-F, Kuang X, Liu K, Zhang H et al (2013) Neuroprotective effect of kaempferol glycosides against brain injury and neuroinflammation by inhibiting the activation of NF- κ B and STAT3 in transient focal stroke. *PLoS ONE* 8:e55839
- Kannurpatti SS, Sanganahalli BG, Herman P, Hyder F (2015) Role of mitochondrial calcium uptake homeostasis in resting state fMRI brain networks. *NMR Biomed* 28:1579–1588
- Parent M, Chitturi J, Santhakumar V, Hyder F, Sanganahalli BG, Kannurpatti SS (2020) Kaempferol treatment after traumatic brain injury during early development mitigates brain parenchymal microstructure and neural functional connectivity deterioration at adolescence. *J Neurotrauma* 37:966–974
- Zhao Y, Tian B, Wang Y, Ding H (2017) Kaempferol sensitizes human ovarian cancer cells-OVCAR-3 and SKOV-3 to tumor necrosis factor-related apoptosis-inducing ligand (TRAIL)-induced apoptosis via jnk/erk-chop

- pathway and up-regulation of death receptors 4 and 5. *Med Sci Monit Int Med J Exp Clin Res* 23:5096–5105
24. Kim TW, Lee SY, Kim M, Cheon C, Ko S-G (2018) Kaempferol induces autophagic cell death via IRE1-JNK-CHOP pathway and inhibition of G9a in gastric cancer cells. *Cell Death Dis* 9:875
 25. Afzal M, Alarifi A, Karami AM, Ayub R, Abduh NAY, Saeed WS et al (2023) Antiproliferative mechanisms of a polyphenolic combination of kaempferol and fisetin in triple-negative breast cancer cells. *Int J Mol Sci* 24:6393
 26. Holland TM, Agarwal P, Wang Y, Leurgans SE, Bennett DA, Booth SL et al (2020) Dietary flavonols and risk of Alzheimer dementia. *Neurology* 94:e1749–e1756
 27. Wan LL, Xia J, Ye D, Liu J, Chen J, Wang G (2009) Effects of quercetin on gene and protein expression of NOX and NOS after myocardial ischemia and reperfusion in rabbit. *Cardiovasc Ther* 27:28–33
 28. Angeloni C, Leoncini E, Malaguti M, Angelini S, Hrelia P, Hrelia S (2008) Role of quercetin in modulating rat cardiomyocyte gene expression profile. *Am J Physiol Heart Circ Physiol* 294:H1233–1243
 29. Nguyen L, Laboissonniere LA, Guo S, Pilotto F, Scheidegger O, Oestmann A et al (2020) Survival and motor phenotypes in FVB C9–500 ALS/FTD BAC transgenic mice reproduced by multiple labs. *Neuron* 108:784–796. e3
 30. Takazawa T, Croft GF, Amoroso MW, Studer L, Wichterle H, Macdermott AB (2012) Maturation of spinal motor neurons derived from human embryonic stem cells. *PLoS ONE* 7:e40154
 31. Mazzoni EO, Mahony S, Closser M, Morrison CA, Nedelec S, Williams DJ et al (2013) Synergistic binding of transcription factors to cell-specific enhancers programs motor neuron identity. *Nat Neurosci* 16:1219–1227
 32. Meyer K, Ferraiuolo L, Miranda CJ, Likhite S, McElroy S, Renusch S, Ditsworth D, Lagier-Tourenne C, Smith RA, Ravits J, Burghes AH, Shaw PJ, Cleveland DW, Kolb SJ, Kaspar BK. Direct conversion of patient fibroblasts demonstrates non-cell autonomous toxicity of astrocytes to motor neurons in familial and sporadic ALS. *Proc Natl Acad Sci U S A*. 2014;111(2):829–832. doi: 10.1073/pnas.1314085111
 33. Gomes I, Sierra S, Devi LA (2016) Detection of Receptor Heteromerization Using In Situ Proximity Ligation Assay. *Curr Protoc Pharmacol* 75:2161–21631
 34. McKenzie M, Lim SC, Duchon MR. Simultaneous measurement of mitochondrial calcium and mitochondrial membrane potential in live cells by fluorescent microscopy. *J Vis Exp*. 2017;55166.
 35. Liu Y, Pattamatta A, Zu T, Reid T, Bardhi O, Borchelt DR et al (2016) C9orf72 BAC mouse model with motor deficits and neurodegenerative features of ALS/FTD. *Neuron* 90:521–534
 36. Bush JA, Aikawa H, Fuerst R, Li Y, Ursu A, Meyer SM et al (2021) Ribonuclease recruitment using a small molecule reduced c9ALS/FTD r(G4C2) repeat expansion in vitro and in vivo ALS models. *Sci Transl Med*. 13:eabd5991
 37. Zu T, Guo S, Bardhi O, Ryskamp DA, Li J, Khoramian Tusi S et al (2020) Metformin inhibits RAN translation through PKR pathway and mitigates disease in C9orf72 ALS/FTD mice. *Proc Natl Acad Sci U S A* 117:18591–18599
 38. Green KM, Glineburg MR, Kearse MG, Flores BN, Linsalata AE, Fedak SJ et al (2017) RAN translation at C9orf72-associated repeat expansions is selectively enhanced by the integrated stress response. *Nat Commun* 8:2005
 39. Cheng W, Wang S, Mestre AA, Fu C, Makarem A, Xian F et al (2018) C9ORF72 GGGGCC repeat-associated non-AUG translation is upregulated by stress through eIF2 α phosphorylation. *Nat Commun* 9:51
 40. Nguyen L, Cleary JD, Ranum LPW (2019) Repeat-associated non-ATG translation: molecular mechanisms and contribution to neurological disease. *Annu Rev Neurosci* 42:227–247
 41. Boyce M, Bryant KF, Jousse C, Long K, Harding HP, Scheuner D et al (2005) A selective inhibitor of eIF2 α dephosphorylation protects cells from ER stress. *Science* 307:935–939
 42. Choi SY, Lopez-Gonzalez R, Krishnan G, Phillips HL, Li AN, Seeley WW et al (2019) C9ORF72-ALS/FTD-associated poly(GR) binds Atp5a1 and compromises mitochondrial function in vivo. *Nat Neurosci* 22:851–862
 43. Silva B, Oliveira PJ, Dias A, Malva JO (2008) Quercetin, kaempferol and biapigenin from *Hypericum perforatum* are neuroprotective against excitotoxic insults. *Neurotox Res* 13:265–279
 44. Wu B, Luo H, Zhou X, Cheng C-Y, Lin L, Liu B-L et al (2017) Succinate-induced neuronal mitochondrial fission and hexokinase II malfunction in ischemic stroke: therapeutic effects of kaempferol. *Biochim Biophys Acta Mol Basis Dis* 1863:2307–2318
 45. Stucki DM, Rueggsegger C, Steiner S, Radecke J, Murphy MP, Zuber B et al (2016) Mitochondrial impairments contribute to Spinocerebellar ataxia type 1 progression and can be ameliorated by the mitochondria-targeted antioxidant MitoQ. *Free Radic Biol Med* 97:427–440
 46. Kouhestani S, Jafari A, Babaei P (2018) Kaempferol attenuates cognitive deficit via regulating oxidative stress and neuroinflammation in an ovariectomized rat model of sporadic dementia. *Neural Regen Res* 13:1827–1832
 47. Oh YK, Shin KS, Yuan J, Kang SJ (2008) Superoxide dismutase 1 mutants related to amyotrophic lateral sclerosis induce endoplasmic stress in neuro2a cells. *J Neurochem* 104:993–1005
 48. Vaccaro A, Patten SA, Aggad D, Julien C, Maios C, Kabashi E et al (2013) Pharmacological reduction of ER stress protects against TDP-43 neuronal toxicity in vivo. *Neurobiol Dis* 55:64–75
 49. Johri A, Chandra A (2021) Connection lost, MAM: errors in ER-mitochondria connections in neurodegenerative diseases. *Brain Sci* 11:1437
 50. Paillusson S, Stoica R, Gomez-Suaga P, Lau DHW, Mueller S, Miller T et al (2016) There's something wrong with my MAM; the ER-mitochondria axis and neurodegenerative diseases. *Trends Neurosci* 39:146–157
 51. Guo W, Yan L, Yang L, Liu X, Gao P et al (2014) Targeting GRP75 improves HSP90 inhibitor efficacy by enhancing p53-mediated apoptosis in hepatocellular carcinoma. *PLoS ONE* 9:085766
 52. Murugan M, Santhakumar V, Kannurpatti SS (2016) Facilitating mitochondrial calcium uptake improves activation-induced cerebral blood flow and behavior after mTBI. *Front Syst Neurosci* 10:19
 53. Brown RH, Al-Chalabi A (2017) Amyotrophic lateral sclerosis. *N Engl J Med* 377:162–172
 54. Hardiman O, Al-Chalabi A, Chio A, Corr EM, Logroscino G, Robberecht W et al (2017) Amyotrophic lateral sclerosis. *Nat Rev Dis Primer* 3:17071
 55. Sasaki S (2010) Endoplasmic reticulum stress in motor neurons of the spinal cord in sporadic amyotrophic lateral sclerosis. *J Neuropathol Exp Neurol* 69:346–355
 56. Smith EF, Shaw PJ, De Vos KJ (2019) The role of mitochondria in amyotrophic lateral sclerosis. *Neurosci Lett* 710:132933
 57. Chen J, Bassot A, Giuliani F, Simmen T (2021) Amyotrophic lateral sclerosis (ALS): stressed by dysfunctional mitochondria-endoplasmic reticulum contacts (MERCs). *Cells* 10:1789
 58. Cozzolino M, Carri MT (2012) Mitochondrial dysfunction in ALS. *Prog Neurobiol* 97:54–66
 59. Kawamata H, Manfredi G (2010) Mitochondrial dysfunction and intracellular calcium dysregulation in ALS. *Mech Ageing Dev* 131:517–526
 60. Das I, Krzyzosiak A, Schneider K, Wrabetz L, D'Antonio M, Barry N et al (2015) Preventing proteostasis diseases by selective inhibition of a phosphatase regulatory subunit. *Science* 348:239–242
 61. Moreno JA, Radford H, Peretti D, Steinert JR, Verity N, Martin MG et al (2012) Sustained translational repression by eIF2 α -P mediates prion neurodegeneration. *Nature* 485:507–511
 62. Vieira FG, Ping Q, Moreno AJ, Kidd JD, Thompson K, Jiang B et al (2015) Guanabenz treatment accelerates disease in a mutant sod1 mouse model of ALS. *PLoS ONE* 10:e0135570
 63. Wu CT, Sheu ML, Tsai KS, Chiang CK, Liu SH (2011) Salubrinal, an eIF2 α dephosphorylation inhibitor, enhances cisplatin-induced oxidative stress and nephrotoxicity in a mouse model. *Free Radic Biol Med* 51:671–680
 64. Shah RS, Walker BR, Vanov SK, Helfant RH (1976) Guanabenz effects on blood pressure and noninvasive parameters of cardiac performance in patients with hypertension. *Clin Pharmacol Ther* 19:732–737
 65. Nishikawa J, Iio M (1986) Diagnosis of metabolic bone diseases: bone scintigraphy. *Nihon Rinsho Jpn J Clin Med* 44:2457–2460
 66. Chen M-C, Hsu L-L, Wang S-F, Pan Y-L, Lo J-F, Yeh T-S et al (2021) Salubrinal enhances cancer cell death during glucose deprivation through the upregulation of xCT and mitochondrial oxidative stress. *Biomedicines* 9:1101
 67. Giorgi C, Baldassari F, Bononi A, Bonora M, De Marchi E, Marchi S et al (2012) Mitochondrial Ca(2+) and apoptosis. *Cell Calcium* 52:36–43
 68. Yang C, Yang W, He Z, Guo J, Yang X, Wang R et al (2021) Kaempferol alleviates oxidative stress and apoptosis through mitochondria-dependent pathway during lung ischemia-reperfusion injury. *Front Pharmacol* 12:624402

69. Montero M, Lobatón CD, Hernández-Sanmiguel E, Santodomingo J, Vay L, Moreno A et al (2004) Direct activation of the mitochondrial calcium uniporter by natural plant flavonoids. *Biochem J* 384:19–24
70. Chu Q, Martinez TF, Novak SW, Donaldson CJ, Tan D, Vaughan JM et al (2019) Regulation of the ER stress response by a mitochondrial microprotein. *Nat Commun* 10:4883
71. Hanaki M, Murakami K, Akagi K, Irie K (2016) Structural insights into mechanisms for inhibiting amyloid β 42 aggregation by non-catechol-type flavonoids. *Bioorg Med Chem* 24:304–313
72. Yan T, He B, Xu M, Wu B, Xiao F, Bi K et al (2019) Kaempferide prevents cognitive decline via attenuation of oxidative stress and enhancement of brain-derived neurotrophic factor/tropomyosin receptor kinase B/cAMP response element-binding signaling pathway. *Phytother Res PTR* 33:1065–1073
73. Yang Y-L, Cheng X, Li W-H, Liu M, Wang Y-H, Du G-H (2019) Kaempferol attenuates LPS-induced striatum injury in mice involving anti-neuroinflammation, maintaining BBB integrity, and down-regulating the HMGB1/TLR4 pathway. *Int J Mol Sci* 20:491

Publisher's Note

Springer Nature remains neutral with regard to jurisdictional claims in published maps and institutional affiliations.